P. Physics

NOV 8 1961

COLE MEMORIAL LIBRARY

SCIENCE OF LIGHT

VOLUME 7 NUMBER 3

December

1958

OHIO STATE UNIVERSITY
NOV 6 - 1961
LIBRARY

Published by the

Institute for Optical Research

Tokyo University of Education

in collaboration with

The Spectroscopical Society of Japan

SCIENCE OF LIGHT

Science of Light contains reports of the Institute for Optical Research and contribution from other science bodies about similar subjects.

The editorial staff consists of following members:

Chairman: Prof. H. Ootsuka, *Tokyo University of Education*

Dr. Y. Fujioka, *Atomic Energy Commission of Japan*

Prof. E. Minami, *University of Tokyo*

Prof. M. Seya, *Tokyo University of Education*

Prof. Y. Uchida, *Kyoto University*

Prof. T. Uemura, *Rikkyo University*

Prof. K. Miyake, *Tokyo University of Education*

All communications should be addressed to the director or to the librarian of the Institute.

The Institute for Optical Research

Tokyo University of Education

400, 4-chome, Hyakunin-machi, Shinjuku-ku, Tokyo, Japan

Printed at
the Printing Department, Chūō Kagakusha,
Tokyo

Properties of Pneumatic Infra-red Detector (I)

Kunio YOSIHARA

Department of Applied Physics, Faculty of Engineering, Nagoya University

(Received December 4, 1958)

Abstract

On the basis of the equation of heat conduction, a mathematical formula is obtained which gives the time constant of the pneumatic cell as a function of the depth of the cell. The numerical calculation of the time constant is carried out with this formula assuming plausible values of various physical constants.

From these results the temperature rise in the cell is calculated under the assumption that the cell has only one time constant. Thus it is ascertained that there is an optimum depth of the cell which gives the maximum temperature rise for a given chopping frequency.

The displacement of a flexible mirror, which is a measure of the sensitivity, is also estimated using the equation of state of the gas and the temperature rise in the cell already obtained, and it is found that, under ordinary conditions, the sensitivity shows a maximum at a certain value of the depth of the cell, which is fairly larger than the value corresponding to the maximum temperature rise.

The pressure dependence of the sensitivity is derived from the combination of the various formulas obtained, and it is shown that the cell has its maximum sensitivity at a pressure between 0.1 and 1 atm.

Lastly, the signal-to-noise ratio of the cell is discussed assuming that there is no noise other than that caused by temperature fluctuation, and the minimum detectable power is also estimated.

1. Introduction

The pneumatic cell invented by M. J. E. Golay[1], being an excellent infra-red detector, is now often used in various fields of infra-red work, especially in the study of the far infra-red. Unfortunately, very few data on its performance are available and one find difficulties in constructing the cell, although Golay[2] has established the fundamental principle of construction.

In this paper, the time constant and the sensitivity of the cell are calculated by directly solving the equation of heat conduction to discuss the important characteristics of the cell and to give the detailed data on its performance.

1) H. H. Zahl and M. J. E. Golay: Rev. Sci. Instr. **17** (1946) 551.
M. J. E. Goay; ibid, **18** (1947) 347; **18** (1947) 357.
2) M. J. E. Golay; Rev. Sci. Instr., **20** (1949) 811.

2. A Rough Estimation of the Time Constant

We shall first calculate the time constant of the cell without the heat absorbing film. (Fig. 1)

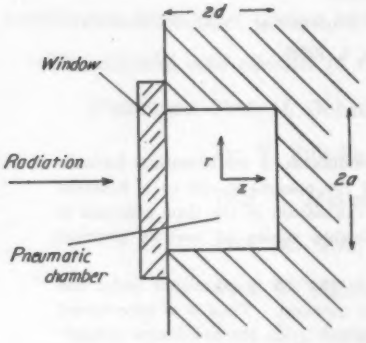

Fig. 1

As will be seen later, the result thus obtained proves to be a fairly good approximation. For simplicity the effect of the narrow duct leading to the flexible mirror as well as of the pneumatic leak is neglected for the calculation.

Consider a cylindrical pneumatic cell, and let its center be the origin of co-odinates, its axis the z-axis. (we shall use hereafter the cyrindrical co-odinates)

The equation for the heat conduction of the gas is given by

$$\frac{\partial(\Delta T_g)}{\partial t}=k\Delta^2(\Delta T_g)$$

where ΔT_g is the temperature rise of the gas above the ambient, k is $\kappa_g/\rho_g c_g$ and κ_g, ρ_g and c_g are the thermal conductivity, the density and the heat capacity per unit mass of the gas respectively.

The boundary conditions in this case are

$$\Delta T_g=0 \quad \text{when} \quad z=\pm d$$
$$\Delta T_g=0 \quad \text{when} \quad r=a$$

where a and d are the radius and the half of the depth of the cylinder respectively. As is well known, the solution of the equation is given by

$$\Delta T_g=\sum_{\mu}\sum_{m}\sum_{n}\exp\left[-k\left(\mu^2+\frac{m^2\pi^2}{4d^2}\right)t\right]$$
$$\times J_n(\mu r)\sin\frac{m\pi}{2d}(z+d)(A_{\mu,m,n}\cos n\theta+B_{\mu,m,n}\sin n\theta)$$

where J_n is the Bessel function of the n-th order, μ is determined by $J_n(\mu\cdot a)=0$, and A's and B's are the constants determined by the initial condition.

This solution shows that the pneumatic cell has an infinite number of time constants (namely the reciprocals of $k(\mu^2+m^2\pi^2/4d^2)$) unlike other infra-red detectors such as thermocouples or bolometers.

In practice, however, when the chopped beam method followed by the electronic amplification is utilized, the largest time constant is the most important so far as the chopping frequency is sufficiently low and the other time constants

are much smaller than the largest. As this condition is nearly satisfied in the present case, we may regard the pneumatic cell as a detector with only one time constant which corresponds to the largest one.

Thus the time constant τ is given by

$$\tau=1/k(\mu_{01}^2+\pi^2/4d^2),\quad \mu_{01}a=2.405 \tag{2}$$

For example, if $\tau=10^{-2}$ sec. and $a=0.15$ cm, d is equal to 9.8×10^{-2} cm for the air-filled cell. Hence we see that, for the pneumatic cell used with the chopped beam method, the depth of the cell must be of the order of 1 mm.

For the "flat cell" for which $a>d$, the equation (2) becomes

$$\tau=\frac{4d^2}{k\pi^2} \tag{2}'$$

3. Calculation of the Time Constant

We now calculate the time constant of the cell with a heat absorbing film within it. Let this film coincide with the xy-plane in Fig. 1.

According to the usual method of solution we assume $\Delta T_g=U(t)\ R(r)\ \Theta(\theta)\ Z(z)$, where U, R, Θ and Z are the functions of t, r, θ and z respectively. From physical considerations ΔT_g must be axially symmetric, and consequently $d^2\Theta/d\theta^2=0$. Thus we have

$$\frac{1}{U}\frac{dU}{dt}=k\left(\frac{1}{R}\frac{d^2R}{dr^2}+\frac{1}{R}\frac{1}{r}\frac{dR}{dr}+\frac{1}{Z}\frac{d^2Z}{dz^2}\right)$$

Put this expression equal to $-k(\alpha^2+\beta^2)$, and let $(1/Z)(d^2Z/dz^2)=-\beta^2$, where α and β are constants. Then we have

$$\frac{dU}{dt}=-k(\alpha^2+\beta^2)U$$

$$\frac{1}{R}\frac{d^2R}{dr}+\frac{1}{R}\frac{1}{r}\frac{dR}{dr}=-\alpha^2$$

$$\frac{1}{Z}\frac{d^2Z}{dz^2}=-\beta^2$$

The particular solution of the problem is given by

$$\Delta T_g=\exp\{-k(\alpha^2+\beta^2)t\}J_0(\alpha r)(c_1\cos\beta z+c_2\sin\beta z) \tag{3}$$

where c_1 and c_2 are constants.

Boundary conditions in this case are

$\Delta T_g=0$ when $z=d$ (4), $\Delta T_g=0$ when $r=a$ (5)

$\Delta T_g=\Delta T_f$ when $z=0$ (6),

$$c_f\frac{d(\Delta T_f)}{dt}=-2\kappa_r\Delta T_f+2\kappa_g\left(\frac{\partial(\Delta T_g)}{\partial z}\right)_{z=0} \tag{7}$$

where ΔT_f is the temperature rise of the absorbing film, c_f is the heat capacity of the film per unit area and κ_r is the radiation cooling constant per unit area. (Note that κ_g and κ_r have different dimensions)

At first sight it seems strange that the condition $\Delta T_g=0$ when $z=-d$ is omitted, but addition of this condition gives rise to a contradiction. This is because the absorbing film has in reality a finite thickness and, strictly speaking, ΔT_g is not zero when $z=-d$ if the origin of the co-ordinates is on the right side of the film. To avoid this difficulty, we consider only the right half of the cell and double both the radiation and conduction losses as shown in the condition (7).

From the condition (4) and (5), ΔT_g given by (3) becomes

$$\Delta T_g=\text{const. } \exp\{-k(\mu_s^2+\beta^2)t\}J_0(\mu_s r)\sin\beta(d-z) \tag{8}$$

where μ_s is determined by $J_0(\mu_s a)=0$.

The condition (6) gives

$$\Delta T_f=\text{const. } \sin(\beta d)\exp\{-k(\mu_s^2+\beta^2)t\}J_0(\mu_s r) \tag{9}$$

Substituting the expression (8) in (7), we have

$$c_f\frac{d(\Delta T_f)}{dt}=-2\kappa_r\Delta T_f-2\kappa_g \text{ const. } \beta\cdot\exp\{-k(\mu_s^2+\beta^2)t\}J_0(\mu_s r) \tag{10}$$

The equations (9) and (10) give

$$c_f\frac{d(\Delta T_f)}{dt}=-\{2\kappa_r+2\kappa_g\beta\cot(\beta d)\}\Delta T_f$$

Therefore

$$\Delta T_f=\text{const.}'\exp\left\{-\frac{2\kappa_r+2\kappa_g\beta\cot(\beta d)}{c_f}t\right\}$$

This equation must be identical with (9). Consequently we have

$$2\kappa_r+2\kappa_g\beta\cot(\beta d)=k(\mu_s^2+\beta^2)c_f$$

This equation determines the constant β. Since the cotangent is a periodic function, there are an infinite number of β's. The general solution for ΔT_g is given by summing up the particular solutions such as (3) with various values of α and β.

Writing $\tau=\{k(\mu_s^2+\beta^2)\}^{-1}$, we have

$$2\kappa_r+2\kappa_g\sqrt{(1/k\tau)-\mu_s^2}\cot(d\sqrt{(1/k\tau)-\mu_s^2})=c_f/\tau$$

or solving for d, we have

$$d=\frac{1}{\sqrt{(1/k\tau)-\mu_1^2}}\operatorname{arccot}\left(\frac{(c_f/\tau)-2\kappa_r}{2\kappa_g\sqrt{(1/k\tau)-\mu_1^2}}\right) \tag{11}$$

From the same reason described in the preceeding section, we are concerned with the largest time constant only. Hence we may put $\mu_s=\mu_1$ and take the principal value of the arccotangent.

For the flat cell for which $a>d$, $\mu_1=0$ and the equation (11) becomes

$$d=\sqrt{k\tau}\,\mathrm{arccot}\left(\frac{(c_f/\tau)-2\kappa_r}{2\kappa_g}\sqrt{k\tau}\right) \tag{12}$$

These equations can be used to calculate d from τ, and allows us to design the cell suitable for our purpose.

We note here that $(1/k\tau)-\mu_1^2$ must not be negative in (11), and thus there exists no cell of which the time constant exdeeds $1/\mu_1^2k$.

4. Approximate Formulas for the Time Constant

In the case of the flat cell we can derive relatively simple formulas for the time constant from the equation (12).

Case 1. $\tau<c_f/2\kappa_r$

Expanding the cotangent, we have

$$d=\sqrt{k\tau}\left\{\frac{\pi}{2}-\left(\frac{\pi}{2}-\frac{2\kappa_g/\sqrt{k\tau}}{(c_f/\tau)-2\kappa_r}-\cdots\right)\right\}=\frac{2\kappa_g}{c_f/\tau-2\kappa_r}$$

Hence

$$\tau=\frac{c_f}{2\kappa_r+(2\kappa_g/d)} \tag{13}$$

The time constant is the heat capacity of the film divided by the total cooling constant. The heat capacity of the gas is in this case so small that it may be neglected.

Case 2. $\tau\fallingdotseq c_f/2\kappa_r$

Expanding the arccotangent in the neighbourhood of zero of the argument, we have

$$\frac{2\kappa_g}{k}d=\frac{\pi}{2}\frac{\tau}{\sqrt{k\tau}}2\kappa_g-c_f+2\kappa_r\tau$$

Solving for τ, we obtain

$$\tau=\frac{c_f+(2\kappa_g d/k)}{2\kappa_r+(\pi/2)(2\kappa_g/\sqrt{k\tau})}.$$

Because τ is approximately equal to $\pi\sqrt{k\tau}/2$ in this case, we have

$$\tau=\frac{c_f+(2\kappa_g d/k)}{2\kappa_r+(\pi/2)^2(2\kappa_g/d)} \tag{14}$$

If we note here that k is $\kappa_g/\rho_g c_g$, $2\kappa_g d/k$ is equal to $2d\rho_g c_g$, which is the heat capacity of the gas per unit cross section. On the other hand, $(\pi/2)^2(2\kappa_g/d)$ represents the "effective" cooling caused by the conduction of heat through the gas. Thus, the physical meaning of the equation (14) is that the time constant

of the cell is the total heat capacity (the heat capacity of the film and the gas) divided by the total cooling constant (the radiation cooling plus the conduction cooling).

Furthermore, it is clear that the equation (14) is reduced to the equation (2)' in the section 2, if $c_f < 2\kappa_g d/k$ and $2\kappa_r < (\pi/2)^2(2\kappa_g/d)$.

Case 3. $\tau > c_f/2\kappa_r$

Using the formula $\operatorname{arccot} x = \pi + \left(\frac{1}{x} + \cdots\right)$ for $x<0$, we have

$$d = \pi(\sqrt{k\pi} - \kappa_g/\kappa_r)$$

Hence

$$\tau = \frac{d^2}{\pi^2 k}\left(1+2\frac{\kappa_g}{d\kappa_r}\right) = \frac{1/2(2dc_g\rho_g)}{\pi^2\kappa_g/d}\left(1+2\frac{\kappa_g/d}{\kappa_r}\right) \tag{15}$$

This equation shows that the time constant is chiefly determined by the heat capacity of the gas and the conduction through the gas, but the radiation cooling is to be taken into account as a correction term.

As these formulas are very simple and have clear physical meaning, they are often useful to anticipate the main characteristics of the pneumatic cell.

5. Numerical Calculation of the Time Constant

In order to evaluate accurately the time constant of the pneumatic cell, we must use the formula (11) or (12). For this purpose, it is necessary to know the physical constants which appear in these formulas.

Since no definite values concerning the physical constants of collodion are available, we assume that the specific heat is 0.4 cal/g deg., the density is 1.5 g/cm^3, and furthermore the thickness is 400 A. Then, the the capacity of collodion film per unit area is 2.4×10^{-6} cal/deg·cm^2. In the present experiment we used antimony as heat absorbing material. The data for antimony are easily found in any physical table. If we assume the thickness of antimony film is 200 A, the heat capacity of antimony becomes 6.65×10^{-7} cal/deg·cm^2.

Thus, for the total heat capacity of the absorbing film per unit area we have

$$c_f = 3.0_6\times10^{-6} \text{ cal/deg·cm}^2$$

As for the gas used in the cell, xenon is the most ideal because it has the smallest thermal conductivity among all kinds of gases suitable for the pneumatic cell. It is, however, interesting to calculate the data for the air-filled cell and to compare them with those of xenon.

Since the gas has two kinds of heat capacity, namely, the heat capacity at constant volume and that at constant pressure, there is some ambiguity as to

which heat capacity is adequate for our purpose. In the present calculation the capacity at constant pressure is employed, because in the actual cell the gas expands to some extent when it is warmed by the incident radiation. There is, however, little difference if the capacity at constant volume is assumed.

Thus, for xenon we have

$$\kappa_g = 1.1 \times 10^{-5} \text{ cal/cm sec. deg.}$$

$$k_g = \frac{\kappa_g}{\rho_g C_g} = 4.96\ 10^{-2} \text{ cm}^2\text{/sec. (at 1 atm.)}$$

and for air we have

$$\kappa_g = 5.65 \times 10^{-5} \text{ cal/cm sec. deg.}$$

$$k_g = \frac{\kappa_g}{\rho_g C_g} = 1.95 \times 10^{-1} \text{ cm}^2\text{/sec. (at 1 atm.)}$$

The radiation colling constant can be easily evaluated using the Stefan-Boltzmann's law and we have

$$\kappa_r = 7.35 \times 10^{-5} \text{ cal/cm}^2 \text{ sec. deg.}$$

where we have assumed that the emissivity of the absorbing film is 0.5.

Once these constants are determined, the dependence of the time constant on the distance between the absorbing film and the wall (d) can be easily calculated numerically from (11) and (12). The results are shown in Fig. 2.

Experimental results so far obtained seem to support this calculation.

It is seen from this figure that, under similar conditions, the xenon-filled cell has a larger time constant than the air-filled cell. But this does not necessarily mean the disadvantage of the former. On the contrary, on account of low thermal conductivity, the temperature rise in the xenon cell becomes much higher, and as will be shown in the following sections, the xenon cell is superior to the air-filled one.

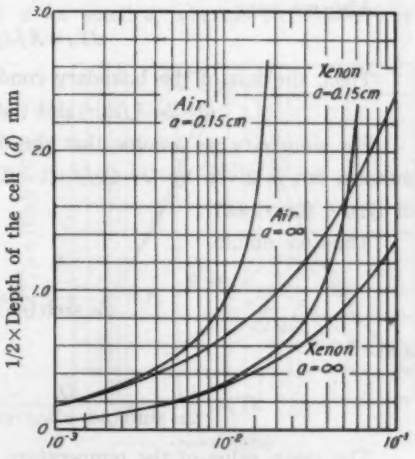

Fig. 2

6. The Mean Value of the Temperature Rise in the Cell

We now proceed to calculate the mean value of the temperature rise in the cell which is of primary importance in the problem of sensitivity, although the

sensitivity depends not only on the temperature rise but also on other factors as will be seen in the next section.

First we calculate the temperature rise for constant incident radiation. The equation to be solved is

$$\left(\frac{\partial^2}{\partial r^2}+\frac{1}{r}\frac{\partial}{\partial r}+\frac{\partial^2}{\partial z^2}\right)(\Delta T_g)=0$$

with the boundary conditions

$$\Delta T_g=0 \quad \text{when} \quad z=d, \qquad \Delta T_g=0 \quad \text{when} \quad r=a,$$
$$\Delta T_g=\Delta T_f \quad \text{when} \quad z=0$$

$$Q=2\kappa_r\Delta T_f-2\kappa_g\left(\frac{\partial(\Delta T_g)}{\partial z}\right)_{z=0}$$

where Q is the power actually absorbed per unit area. (Q is in general a function of r)

Using a similar procedure as in the section 3, we have

$$\Delta T_g=A\cdot J_0(\mu r)\sinh\{\mu(d-z)\}$$

where μ is given by $J_0(\mu a)=0$, and A is a constant.

Also we have

$$\Delta T_f=AJ_0(\mu r)\sinh(\mu d)$$

Then, the last of the boundary conditions becomes

$$Q=2\kappa_r AJ_0(\mu r)\sinh(\mu d)+2\kappa_g AJ_0(\mu r)\mu\cosh(\mu d)$$

For simplicity we assume that the distribution of the incident radiation is not uniform but is given by $Q=Q_0J_0(\mu r)$. (Otherwise Q must be expanded in a series of Bessel functions)

Thus we obtain

$$A=\frac{Q_0}{2\kappa_r\sinh(\mu d)+2\kappa_g\mu\cdot\cosh(\mu d)}$$

and

$$\Delta T_g=\frac{Q_0}{2\kappa_r\sinh(\mu d)+2\kappa_g\mu\cdot\cosh(\mu d)}J_0(\mu r)\sinh\{\mu(d-z)\}$$

The mean value of the temperature rise in the cell is given by

$$\overline{(\Delta T_g)_0}=\frac{Q_0}{2\kappa_r\sinh(\mu d)+2\kappa_g\cdot\mu\cdot\cosh(\mu d)}$$
$$\times\frac{1}{\pi a^2 d}\int_0^a J_0(\mu r)\cdot 2\pi r\cdot dr\int_0^d\sinh\{\mu(d-z)\}dz$$
$$=Q_0\frac{2J_1(\mu a)}{\mu a}\cdot\frac{\cosh(\mu d)-1}{\mu d\sinh(\mu d)}\cdot\frac{1}{2\kappa_r+2\kappa_g\mu\cdot\coth(\mu d)} \tag{16}$$

For the flat cell we have

$$(\overline{\Delta T_g})_0=\frac{Q_0}{2}\frac{2J_1(\mu a)}{\mu a}\frac{1}{2\kappa_r+2\kappa_g/d} \tag{17}$$

In these formulas, the suffix 0 of ΔT_g means that the chopping frequency is zero.

In the case of the flat cell, if the incident radiation is uniform over the absorbing film, we have by a simple calculation

$$(\overline{\Delta T_g})_0=\frac{Q_0}{2}\frac{1}{2\kappa_r+2\kappa_g/d}$$

This is different from (17) by a factor $2J_0(\mu a)/\mu a$. The difference arises from the fact that the incident radiation is assumed non-uniform in the above calculation.

If we assume that the pneumatic cell has only one time constant given in the preceeding section, the estimation of response for chopped incident radiation can be carried out easily as in the case of thermocouples or bolometers. The result is

$$(\overline{\Delta T_g})_\nu=(\overline{\Delta T_g})_0\frac{1}{\sqrt{1+(2\pi\nu\tau)^2}} \tag{18}$$

where ν is the chopping frequency.

$(\overline{\Delta T_g})_0$ is an increasing function of d for small d, whereas $1/(1+(2\pi\nu\tau)^2)$ is a decreasing function because τ increases with d. Consequently $(\overline{\Delta T_g})_\nu$ becomes maximum at a certain value of d. Thus we see there is an optimum depth of the cell for a given chopping frequency.

In Fig. 3 $(\overline{\Delta T_g})_\nu$ given by (18) is plotted against d assuming $Q_0=10^{-2}$ cal/cm^2 and $\nu=10$ c/s. The thickness of the absorbing film, the physical constants, etc. are the same as used in the section 5.

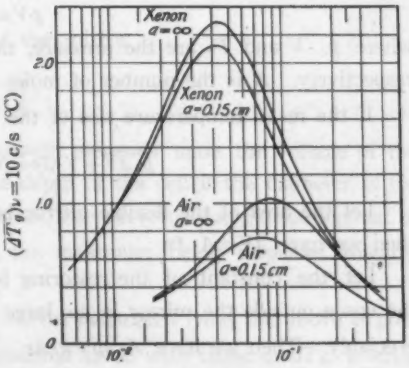

Fig. 3

This figure shows that the xenon cells are decidedly more advantageous than the air ones so far as the mean temperature rise is concerned. Furthermore, the loss due to finite diameter of the cell is not so serious as was first expected, especially for the xenon cells. Thus we see that the increase of diameter makes little gain in the mean temperature rise as far as the distribution of the incident radiation over the absorbing film is similar.

Unfortunately, these calculations cannot be verified experimentally, because it is difficult to construct similar cells except the depth, and furthermore there is no

means to measure directly this temperature rise of the gas.

We must note here that the equation (18) is not valid for all values of d. The wave-length of the heat wave generated by periodical irradiation becomes shorter with increasing frequency, and when it finally becomes smaller than the depth of the cell, maxima and minima of temperature appear in the cell and it becomes impossible to regard the cell as a detector with only one time constant. In the calculation above, where the chopping frequency is 10 c/s, the wave-length of the heat wave is about 5 mm for air and 2 mm for xenon. Thus we see that the equation (18) is a good approximation at least in the neighbourhood of the maximum in Fig. 3, though near the right ends the curves do not correctly represent the real behavious of the cell.

7. Sensitivity of the Cell

The pneumatic cell is the more sensitive the larger the displacement of the flexible mirror is, provided that the intensity of the incident radiation is the same. Hence we may take this displacement as the measure of sensitivity.

We now consider how this displacement depends on various parameters of the cell.

The equation of state of the gas is

$$pV=NRT_g$$

where p, V and T_g are the pressure, the volume and the temperature of the gas respectively. N is the number of moles and R is the gas constant.

If the mean temperature rise of the gas is $\overline{\Delta T_g}$, we have

$$p\cdot\Delta V+V\cdot\overline{\Delta p}=NR\overline{\Delta T_g}=\frac{pV}{T}\overline{\Delta T_g}$$

Let the area of the flexible mirror be A and its effective displacement be Δx, then we have $\Delta V=A\cdot\Delta x$.

Let the constant of the restoring force of the mirror be α, and assume that the space outside the mirror is so large that its pressure does not change appreciably. Then we have $A\cdot\overline{\Delta p}=\alpha\cdot\Delta x$.

From these relations it follows that

$$\Delta x=\frac{Ap\cdot\overline{\Delta T_g}}{T(\alpha+pA^2/V)} \tag{19}$$

Strictly, the above discussion is valid only for constant incident radiation, but the natural frequency of the mirror is so high when compared with the usual chopping frequency that these formulas are practically good approximations. (The natural frequency can be evaluated using the data for surface tension obtained by Golay.)

From the expression (19) we can calculate the sensitivity of the cell as follows.

Case 1. Flat cell

In this case the diameter and consequently the volume of the cell are so large that PA^2/V is neglibible as compared with α. Then we have

$$\Delta x=\frac{Ap\cdot\overline{\Delta T_\theta}}{T\alpha}$$

If A, p, T and α are fixed, Δx is proportional to $\overline{\Delta T_\theta}$.

Case 2. Cell with finite diameter

In this case the term pA^2/V becomes important as is seen by the following estimations.

The restoring force consists of the elastic force and the surface tension of the film. As the flexible mirror is made of extremely thin membrane, the elastic force may be negligible when compared with the surface tension. If this is the case, the constant of the restoring force α proves to be simply $4\pi\Gamma$ by an elementary calculation, where Γ is the constant of the surface tension. According to Golay Γ is of the order of 10^3 dynes/cm, whence $4\pi\Gamma$ is of the order of 10^4 dynes/cm. On the other hand, PA^2/V is about 2.4×10^5 dynes/cm at 1 atm., assuming that $a=d=0.15$ cm and $A=7\times10^{-2}$ cm^2. Thus we see that $4\pi\Gamma$ is generally fairly smaller than PA^2/V.

Then we have for the displacement of the mirror

$$\Delta x=\frac{V\cdot\overline{\Delta T_\theta}}{TA}$$

We find that in this case the sensitivity depends upon the volume of the cell, and in particular it depends upon the depth of the cell if the diameter of the cell is fixed. On account of this dependence, the curve of Δx, plotted against d, becomes very different from that of $\overline{\Delta T_\theta}$, the maximum being displaced towards a larger value of d.

In Fig. 4 are shown the sensitivity curves calculated from the above expressions. For the flat cells the positions of maxima agree with those of $\overline{\Delta T_\theta}$, whereas for the cells with finite diameters the maxima occur at about 1.5 mm, though they are not so distinct.

We must remember that, as was pointed out in the preceeding section, the curves in Fig. 3 and accordingly the curves in Fig. 4 do not represent the real behaviour of the cell near the right ends. Therefore, it is a question whether the maxima of the curves in Fig. 4 correspond precisely to the real maxixa of the sensitivity. Perhaps the sensitivity will fall more rapidly than these curves when α exceeds 1 or 2 mm, because the temperature distribution begins to show a

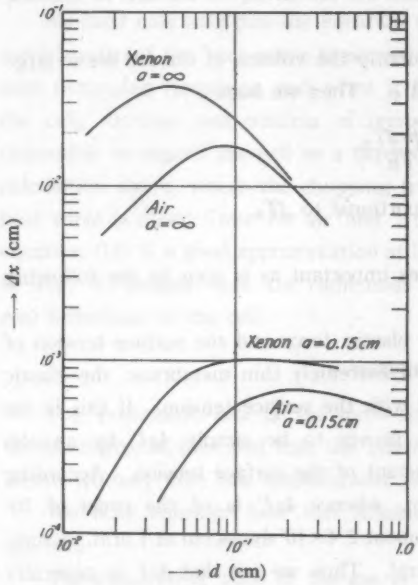

Fig. 4

minimum near the wall of the cell, and as a result of this, the positions of these mixima will be somewhat displaced to the left. But a more exact calculation is necessary to get correct sensitivity curves.

Usually we employ the pneumatic cell instead of thermocouples when the incident beam has so large a cross section that the thermocouple cannot utilize all of the incident power on account of its small receiving area, as is the case with the far infra-red spectrometer. In such a case it seems advantageous to make the area of the absorbing film just equal to the cross section of the incident beam, because the sensitivity increases remarkably with increase of the diameter of the cell as shown in Fig. 4. We must be careful, however, to distinguish the sensitivity from the signal-to-noise ratio. It is because the factor $Ap/T\ (\alpha+pA^2/V)$ in (19) becomes large that the flat cell has a greater sensitivity than that of the cell with finite diameter. But, for the same reason, the fluctuation of temperature in the cell (temperature noise etc.) gives rise to a large random displacement of the flexible mirror. Hence, increase of the factor $Ap/T(\alpha+pA^2/V)$ does not mean the improvement of the signal-to-noise ratio. This ratio is limited in principle by the temperature fluctuation in the cell itself, if there is no other kind of fluctuation.

The signal-to-noise ratio of the cell will be discussed later.

8. Effect of Gas Pressure on the Sensitivity

It is interesting to investigate the dependence of the sensitivity on the gas pressure in the cell. Indeed, this dependence is generally very much complicated and it is almost impossble to estimate it exactly, but some qualitative conclusions can be obtained by applying the formulas already derived.

Let the chopping frequency ν and the depth of the cell be fixed, and let the gas pressure only be variable. For simplicity we shall use the expression (14) for the time constant and the expression (17) for $(\Delta T_0)_0$, even when the diameter of the cell is not very large.

We must remember that the heat conductivity of the gas does not depend on the pressure so far as the pressure is higher than the range in which molecular flow takes place.

(1) Cell with finite diameter

Low frequency operation

When the chopping frequency is sufficiently low, namely $(2\pi\nu\tau)^2 \ll 1$, we have from (18) and (19)

$$\Delta x \propto \frac{1}{2\kappa_r + 2\kappa_g/d} \frac{Ap}{T(\alpha + pA^2/V)} \tag{20}$$

The time constant does not appear in this expression. When the gas pressure p is higher than 1 atm., α is small as compared with pA^2/V and we have

$$\Delta x \propto \frac{1}{2\kappa_r + 2\kappa_g/d} \frac{V}{TA}$$

As κ_g is independent of p in this range, Δx must be nearly constant.

Since α is about one tenth of pA^2/V, α cannot be neglected when p approaches 10^{-1} atm., and then Δx begins to decrease.

When the pressure is considerably below 10^{-1} atm. but is greater than the range of molecular flow, the expression (20) becomes

$$\Delta x \propto \frac{1}{2\kappa_r + 2\kappa_g/d} \frac{Ap}{T\alpha}$$

Thus we see that Δx decreases linearly with the decreasing pressure in this region.

As the diameter of the cell is of the order of one millimeter, the molecular flow begins to occur at about 10^{-4} atm., and the heat conductivity κ_g also begins to decrease. As a result of this, the rate of decrease of Δx becomes somewhat smaller.

If the pressure is reduced further, the heat conductivity becomes so small that it can be neglected as compared with radiation cooling. Thus we have

$$\Delta x \propto \frac{1}{2\kappa_r} \frac{Ap}{T\alpha}$$

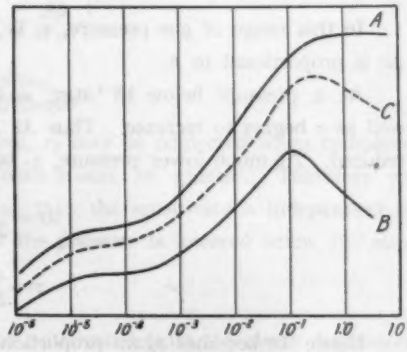

Fig. 5

Hence, Δx decreases again linearly with decreasing pressure.

The curve A in Fig. 5 indicates such a variation of sensitivity with pressure as a whole.

High frequency operation

In this case $(2\pi\nu\tau)^2>1$, and it follows from (18) and (19) that

$$\Delta x=\frac{1}{2\kappa_r+2\kappa_g/d}\frac{Ap}{T(\alpha+pA^2/V)}\frac{1}{\tau}$$

where τ is given by

$$\tau=\frac{c_f+2dc_g\rho_g}{2\kappa_r+(\pi/2)^2(2\kappa_g/d)}$$

according to (14). In this expression, $2d\rho_g c_g$ proves to be about ten times greater than c_f at 1 atm. if d is about 1.5 mm. Hence, when p is greater than 10^{-1} atm., we have $\tau\propto\rho_g\propto p$. On the other hand we have $\alpha<pA^2/V$ as in the previous case. Thus it follows that

$$\Delta x\propto\frac{1}{2\kappa_r+2\kappa_g/d}\frac{V}{TA}\frac{1}{p}$$

Since κ_g is independent of p in this range, Δx is inversely proportional to the gas pressure.

When $10^{-4}<p<10^{-1}$ atm., α and c_f are far greater than pA^2/V and $2dc_g\rho_g$ respectively. Then we have

$$\Delta x\propto\frac{1}{2\kappa_r+2\kappa_g/d}\frac{Ap}{T\alpha}\frac{1}{\tau}$$

$$\tau=\frac{c_f}{2\kappa_r+(\pi/2)^2(2\kappa_g/d)}$$

In this range of gas pressure, κ_g is independent of pressure and consequently Δx is proportional to p.

At a pressure below 10^{-4} atm., κ_g begins to decrease, whence $1/(2\kappa_r+2\kappa_g/d)$ as well as τ begins to increase. Thus Δx decreases more slowly as the pressure is reduced. At much lower pressure, κ_g becomes so small that we have

$$\Delta x\propto\frac{1}{2\kappa_r}\frac{Ap}{T\alpha}\frac{1}{\tau}$$

$$\tau=\frac{c_f}{2\kappa_r}$$

Hence Δx becomes again proportional to the gas pressure. The curve B shows the variation of sensitivity in this case.

Intermediate frequency operation

In actual cases, $(2\pi\nu\tau)^2$ has a value comparable with 1 and the pressure dependence of sensitivity becomes complicated. But the curve representing this dependence must lie between the curves A and B in Fig. 5. Thus the broken

curve such as C may be used as a rough approximation. We may expect from the general tendency of this curve that the pneumatic cell has a maximum sensitivity at a pressure between 10^{-1} and 1 atm., though this maximum is presumably not very conspicuous.

(2) Flat cell

In the above discussion we have assumed that the diameter of the cell is not very large but large enough to permit the application of the expressions (14) and (17). For the flat cell the situation is fairly different. In this case the volume V becomes very large owing to the large diameter even if the thickness of the cell is small. Hence α is large when compared with pA^2/V in (19) and we have

$$\Delta x=\frac{A\cdot p\cdot\sqrt{\Delta T_g}}{T\alpha} \tag{21}$$

Low frequency operation

As $(2\pi\nu\tau)^2$ is by far smaller than 1, we have from (21)

$$\Delta x\propto\frac{1}{2\kappa_r+2\kappa_g/d}\,\frac{Ap}{T\alpha}$$

We can see from this expression that the sensitivity is proportional to the pressure near 1 atm., and becomes constant when the pressure is so large that pA^2/V exceeds α. But in practice such a high pressure cannot be attained.

High frequency operation

In this case we have

$$\Delta x\propto\frac{1}{2\kappa_r+2\kappa_g/d}\,\frac{Ap}{T\alpha}\,\frac{1}{\tau}$$

$$\tau=\frac{c_f+2dc_g\rho_g}{2\kappa_r+(\pi/2)^2(2\kappa_g/d)}$$

From the same reason described above, c_f may be neglected when compared with $2dc_g\rho_g$ if the pressure is comparable with 1 atm. or greater. Therefore we have as before $\tau\propto\rho_g\propto p$. As a result of this, the sensitivity is independent of pressure in this range. It is not until the pressure is lowered below 10^{-1} atm. that the sensitivity begins to decrease.

Intermediate frequency operation

In this case the sensitivity curve can be anticipated from the above discussion. We may conclude that the sensitivity will increase with increase of gas pressure of the cell.

9. Signal-to-noise Ratio and Minimum Detectable Power

The most significant criterion for the infra-red detector is the signal-to-noise

ratio rather than the sensitivity itself. For thermocouples or bolometers, this ratio is chiefly limited by the Johnson noise, although the temperature noise becomes important in certain conditions. Unfortunately the origin of the noise other than the temperature is not well investigated for the pneumatic cell. Indeed Smith and others[3] pointed out that the damping of the motion of the flexible mirror gives rise to a kind of undesirable noise, but the amount of this noise cannot be estimated numerically because the nature of the damping are not clear. Hence we assume for the present that there is no noise except that caused by the temperature fluctuation, and discuss the results derived under this assumption.

The mean temperature fluctuation $\overline{\Delta T_{\text{noise}}}$ is given by[4]

$$\overline{(\Delta T_{\text{noise}})^2}=\frac{4kT^2\kappa\Delta\nu}{\kappa^2+(2\pi\nu C)^2} \tag{22}$$

where k is the Boltzmann constant, κ is the total cooling constant, C is the total heat capacity and $\Delta\nu$ is the frequency bandwidth. In the present case it is more reasonable to calculate κ using the expression $\kappa=C/\tau$ than to calculate it directly, because the pneumatic cell is assumed to have only one time constant.

Thus (22) becomes

$$\overline{(\Delta T_{\text{noise}})^2}=4kT^2\frac{(\tau/C)\Delta\nu}{1+(2\pi\nu\tau)^2}$$

Then we have for the signal-to-noise ratio S/N

$$S/N=\frac{\overline{(\Delta T_g)_\nu}}{\sqrt{\overline{(\Delta T)^2_{\text{noise}}}}}=\frac{1}{\sqrt{4kT^2\Delta\nu}}\overline{(\Delta T_g)_0}(C/\tau)^{1/2} \tag{23}$$

Remembering that $C=\pi a^2c_f+2d(\pi a)^2\rho_g c_g$, S/N can be evaluated numerically with this expression. The results are shown in Fig. 6 in which S/N is plotted against d, assuming $a=0.15$ cm, $Q_0=10^{-2}$ cal/sec. cm^2 and $\Delta\nu=1$ c/s.

It is seen from this figure that there is an optimum depth which gives the largest signal-to-noise ratio. This depth is somewhat smaller than that corresponding to the maximum sensitivity but is larger than that corresponding to the maximum of $\overline{(\Delta T_g)_\nu}$.

In the case of the cell with a large receiving area, however, we are chiefly concerned with the variation of S/N with the area of the absobing film, for such a cell is usually employed to measure a beam with large cross section. Let the area of the absorbing film be E, then κ and C are proportional to E, and accord-

3) R. A. Smith, F. E. Jones and R. P. Chasmar; The Detection and Measurement of Infra-red Radiation. Oxford at the Clarendon Press (1957) p. 278.

4) ibid. p. 206.

ingly the mean temperature fluctuation is inversely proportional to $\sqrt{E}$. On the other hand, it is seen from Fig. 3 that $\overline{(\Delta T_g)_v}$ will be nearly constant when E becomes fairly large. Thus we find that the signal-to-noise ratio is approximately proportional to the square root of the receiving area for the flat cell.

The effect of gas pressure on the signal-to-noise ratio is interesting. The signal-to-noise ratio is given by (23) as before. If we use the simplified expression (14) for the time constant τ and remember that the numerator of (14) is the heat capacity per unit cross section, we obtain

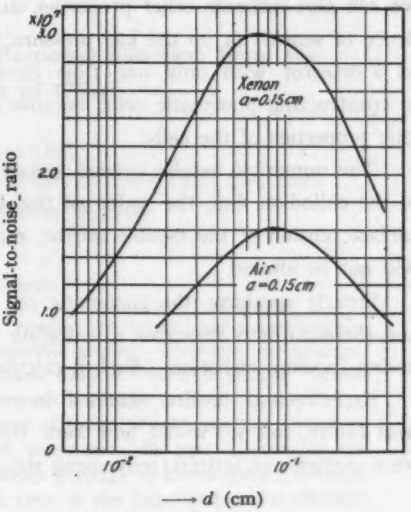

Fig. 6

$$S/N=\frac{1}{\sqrt{4kT^2\Delta\nu}}\frac{Q_0J_1(\mu a)}{\mu a}\frac{\{2\kappa_r+(\pi/2)^2(2\kappa_g/d)\}^{1/2}E^{1/2}}{2\kappa_r+2\kappa_g/d}$$

This expression does not contain any quantity which depends upon the pressure so far as the pressure is higher than the range where the molecular flow occurs. Thus the change of pressure has no effect on the signal-to-noise ratio of the cell. Indeed, use of more exact expression of τ may show some depencence of S/N on p, but we may conclude that this depencence is very small.

The minumum detectable power can be calculated easily from Fig. 6. We assume here that this power is given by the condition $S/N=1$. If we use the cell in the optimum condition and remember that the absorptive power of the receiving film is 0.5 and the distribution of the incident power is given by $Q_0 \times J_0(\mu_1 r)$, we obtain the minimum detectable power as 8.6×10^{-11} watt for the xenon cell and 1.6×10^{-10} watt for the air cell, provided that the diameter is each 3 mm. The value for xenon cell agrees approximately with that obtained by Golay. Therefore the minimum detectable power of the pneumatic cell seems to be limited chiefly by the temperature noise. But more detailed investigations are necessary about this problem.

10. Summary

Starting from the equation of heat conduction, we are able to calculate the time constant and the sensitivity of the pneumatic cell, and using these results,

we can also estimate other properties such as the signal-to-noise ratio, the dependence of sensitivity on the gas pressure, etc., so far as the cell can be regarded as a detector with only one time constant. These calculations will be useful in constructing pneumatic cells, because it is possible to anticipate the characteristic properties of the cells.

The numerical results depend indeed upon the assumption about the thicknes of the collodion film, the value of the specific heat of collodion, the value of the surface tension of the flexible mirror, etc., but the essential part of the discussion will not be altered.

Strictly speaking, the pneumatic cell has an infinite number of time constants and therefore it is desirable to calculate more rigorously the response to the alternating incident radiation. Such a calculation will be published in another paper.

Experimental results obtained in our laboratory will be also published in the near future, but we would add here that recordings of many infra-red spectra were carried out satisfactorily using the pneumatic cell constructed by the author.

11. Acknowledgement

The author wishes to express his sincere thanks to Professor T. Suga for his kind encouragement and guidance, and to Assistant Professor I. Ninomiya of the department of applied mathematics for his helpful advice in the mathematical treatment of the problem of heat conduction.

On the Measurement of Response Function from the Contrast of Chart

Teruji Ose
Institute of Industrial Science, University of Tokyo, Chiba City, Japan
(Received November 12, 1958)

Synopsis

Response function of an optical system can be obtained experimentally from the contrast of image of a sinusoidal grating. However, in practice, either "finite grating" with two or three lines or "variable grating" whose constant varies stepwise from point to point is usually employed.

The author examines if the contrast of image of such gratings gives true response function of the optical system under test. In part I, error of the response function obtained from "variable grating" is shown and the criterion for the grating is given. In part II, error of the response function obtained from "finite greating" is shown analytically.

1. Introduction

In is well known that the response function (contrast transmission factor) of an optical system can be obtained experimentally from the contrast of the image of a sinusoidal grating as follows:

Transmittance or reflectance of a sinusoidal grating with black background across its lines is given by

$$A(x)=\frac{1}{2}(1+\cos f(x))$$

where $f(x)$ is a modulation function, its derivative being the instantaneous angular frequency $\omega(x)$, that is:

$$\frac{df}{dx}=\omega(x) \qquad (1)$$

In a regular sinusoidal grating, as $\omega(x)$ is constant,

$$f(x)=\omega_0 x$$

where $\omega_0=2\pi/\lambda_0$, λ_0 being the wavelength.

If the impulse response of an optical system, the intensity distribution of the image of an infinitely thin line at the center of the field, is $h(x)$, the intensity distribution of the image of the regular sinusoidal grating is by assuming magnification of the optical system as 1

$$B(y)=\frac{1}{2}\left[1+\int_{-\infty}^{+\infty}h(x)\cos\omega_0(y-x)dx\right] \qquad (2)$$

If we put

$$\int_{-\infty}^{+\infty}h(x)dx=1 \quad \text{and} \quad C_0=\int_{-\infty}^{+\infty}h(x)\cos\omega_0 x dx, \quad S_0=\int_{-\infty}^{+\infty}h(x)\sin\omega_0 x dx \qquad (3)$$

then

$$B(y)=\frac{1}{2}\left[1+C_0\cos\omega_0 y+S_0\sin\omega_0 y\right]$$

Accordingly, contrast of the image is,

$$R(\omega_0)=\frac{B_{\max}-B_{\min}}{B_{\max}+B_{\min}}=\sqrt{C_0^2(\omega_0)+S_0^2(\omega_0)} \qquad (4)$$

On the other hand, the response function of an optical system is defined as the Fourier transform of $h(x)$, that is,

$$H(\omega_0)=\sqrt{C_0^2(\omega_0)+S_0^2(\omega_0)}\exp\left[i\tan^{-1}\frac{S_0(\omega_0)}{C_0(\omega_0)}\right] \qquad (5)$$

So the absolute value and the phase of the response function can be obtained from the contrast and the shift of the image[1].

But, in this method, to find the response function for various ω_0, numerous gratings of different constants must be used. Moreover, these gratings should be extended to infinite at both sides to avoid the end effect (explained below). To save these troubles, a grating, the constant of which varies continuously from

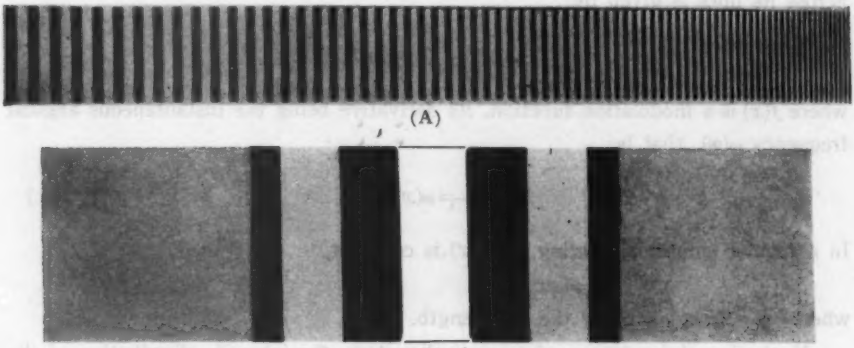

Fig. 1. (A) Variable grating.
(B) Finite grating with black background and gray surround.

1) e. g. Lindberg: Optica Acta **1** (1954) 80.

point to point[2] (e. g. Fig. 1 (A)), and a grating of finite length[3] (e. g. Fig. 1 (B)) are being used. But, with such gratings, we can no longer put ω_0=const. in (4) in the former case and the upper and lower limits of integral in (3) are not infinite in the latter case. Accordingly, C_0 and S_0 in (3) are no longer equal to C_0 and S_0 in (5) and, strictly speaking, $H(\omega_0)$ can not be obtained from the contrast of the image. But, as such gratings are being used extensively in practice, it is very necessary to examine with what degree of accuracy $H(\omega_0)$ is obtainable from the contrast of the image of these gratings.

As a variable grating corresponds to a frequency modulated carrier and a finite grating to an amplitude modulated carrier in terms of radio communication, we shall examine the end effects mentioned above for the case of variable grating in part I and for the case of finite grating in part II by these correlations.

Part I. Response function obtained from the image of a variable grating

§ 2. General formula

In the case of variable grating, (2) becomes

$$B(y)=\frac{1}{2}\left[1+\int_{-\infty}^{+\infty}h(x)\cos f(y-x)dx\right] \tag{6}$$

But, as $h(x)$ is very small when x is larger than a certain value p, where p is about half the width of the image of a thin line, we can replace the upper and lower limits of the integral with p. Hence, if $y>p$, then $y>x$, and $f(y-x)$ can be expanded into Taylor series as

$$f(y-x)=f(y)-x\cdot f'(y)+\frac{1}{2}x^2\cdot f''(y)$$

If we neglect the terms higher than x^2, we get

$$\int_{-\infty}^{+\infty}h(x)\cos f(y-x)dx\fallingdotseq C\cos f(y)+S\sin f(y)$$

where,

$$C=\int_{-\infty}^{+\infty}h(x)\cos\left(f'(y)\cdot x\right)dx,\qquad S=\int_{-\infty}^{+\infty}h(x)\sin\left(f'(y)\cdot x\right)dx$$

and (6) becomes

$$B(y)\fallingdotseq\frac{1}{2}\left[1+\sqrt{C^2+S^2}\cos\left(f(y)-\varphi\right)\right] \tag{7}$$

---

2) K. Murata and H. Matsui: J. App. Phys. Japan **25** (1956) 456.

3) O. H. Shade: N. B. S. circular. **526** (1954) 231.

where

$$\varphi=\tan^{-1}(S/C)$$

As $f'(x)$ is the instantaneous frequency $\omega(x)$ from (1), we can see in the case of variable grating that the contrast and the shift of the image also give the absolute value and phase of response function approximately. Error due to the use of variable grating is the result of neglecting the terms higher than x^2.

§ 3. Modulation function

Below, the accuracy of response function obtained from (7) is examined with some examples.

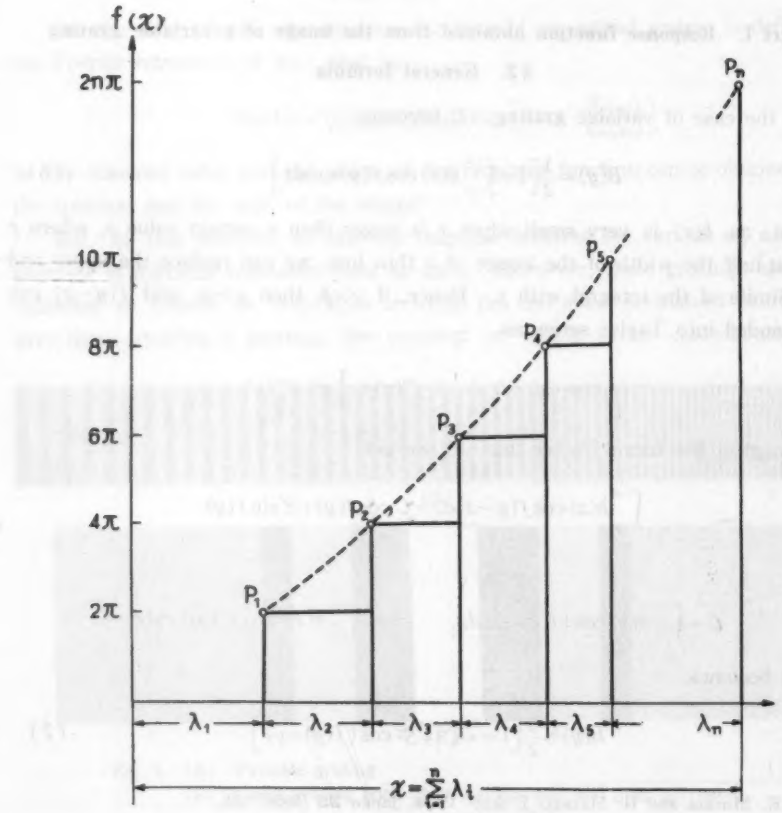

Fig. 2. Modulation function.

Arith Prog
a, a+d, a+2d, a+3d, ...
a = 1st Term
d = common diff
n = no of Terms
ℓ = last Term
S = sum of n Terms

$\ell = a+(n-1)d$

$S = \frac{n}{2}(a+\ell)$

In the case of frequency varying as a linear function of x (i.e. N.B.S.-type chart[4]),

$$\omega(x)=2mx+l$$

The modulation function is simply given from (1) as

$$f(x)=mx^2+lx+c \tag{8}$$

But in most variable gratings used in practice, frequency or pitch varies discontinuously as is shown in Fig. 1 (A). Accordingly, the modulation function is not a continuous function but a step function as is shown with full line in Fig. 2. At each of the steps $P_1, P_2, P_3, \cdots P_n$, x and $f(x)$ are given as

$$x=\sum_{i=1}^{n}\lambda_i, \qquad f(x)=2n\pi \qquad n\text{: integer} \tag{9}$$

As it is hardly possible to treat such a step function analytically, we shall use a continuous function for it as is shown by a broken line in the same figure obtained by eliminating integer n as follows:

(i) When the pitch varies in geometrical progression, we heve for (9)

$$x=\lambda_0(1-k^n)/(1-k), \qquad f_g(x)=2n\pi$$

where λ_0 is the first term and k is the common ratio of the progression.

The modulation function in this case is, by eliminating n,

$$f_g(x)=\{2\pi/\log k\}\{\log(1-(1-k)x/\lambda_0)\} \tag{10}$$

(ii) When the pitch varies in arithmetical progression, we have by putting the common difference as d and the first term as λ_0

$$x=n\{2\lambda_0+(n-1)d\}/2,, \qquad f_a(x)=2n\pi,$$

Thus the modulation becomes:

$$f_a(x)=\{\pi(2\lambda_0-d)/d\}\{\sqrt{1+8xd/(2\lambda_0-d)^2}-1\} \tag{11}$$

In the case $k=1$ or $d=0$, both are reduced to

$$\lim_{k\to 1} f_g(x)=\lim_{d\to 0} f_a(x)=2\pi x/\lambda_0$$

§ 4. Numerical examples

The response function is calculated in the case of defocus by assuming $h(x)$ to be a square shape pulse of width $2p$, that is

$$\begin{aligned} h(x)&=1/2p \qquad |x|\leq p \\ h(x)&=0 \qquad |x|>p \end{aligned} \tag{12}$$

(a) Geometrical progression grating

The modulation function of the grating in this case is (10), but without losing its generality, it can be put as

4) F. E. Washer and F. W. Rosberry: J. Opt. Soc. Am. **41** (1951) 597.

a, ar, ar², ar³

a = 1st Term
r = common ratio
n = no. of Terms
l = last Term
S_n = Sum of n Terms

$l = ar^{n-1}$

$S_n = a\left(\frac{r^n-1}{r-1}\right) = \frac{rl-a}{r-1}$

if $r^2<1$ $\quad S_n \xrightarrow[n\to\infty]{} S_\infty = \frac{a}{1-r}$

$$f_g(x)=A\log x, \qquad A=2\pi/\log k$$

Accordingly, the instantaneous frequency is

$$f_g'(x)=A/x=A/y.$$

Intensity distribution of the image is by putting above formulas into (2)

$$B(y)=\frac{1}{2}\left\{1+\left[\{x/p(1+A^2)\}\cos(A\log x)+p\sin(A\log x)\right]_{y-p}^{y+p}\right\}$$

So, the contrast is given as follows:

$$R(\omega)=\{\sin\beta/p\omega\}\{A/\sqrt{1+A^2}\}\sqrt{1+(p\omega/A)^2\cot^2\beta}$$

where

$$\beta=A\log[(1+p\omega/A)/(1-p\omega/A)]/2 \tag{13}$$

Results of calculation when $k=1.1$ and $p=0.03$, 0.06, 0.09, and 0.12 are shown with ○, ×, □ and △, respectively in Fig. 3.

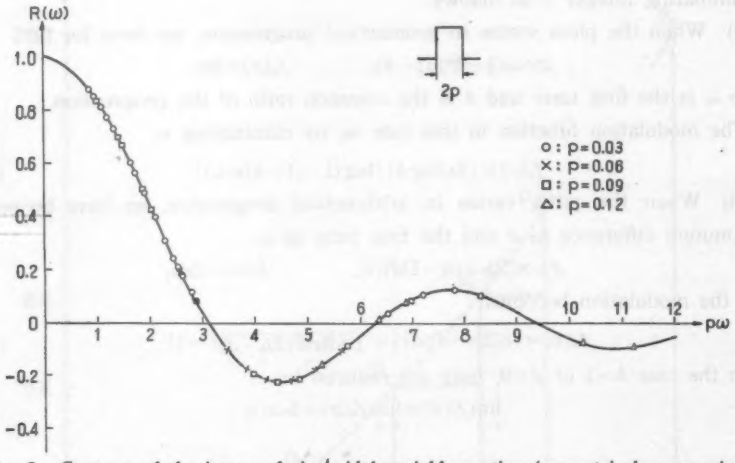

Fig. 3. Contrast of the image of sinusoidal variable grating (geometrical progression). Full line denotes correct response function.
○, ×, □ and △ show calculated contrasts for $p=0.03$, $p=0.06$, $p=0.09$ and $p=0.12$, respectively.

The response function in this case should be

$$H(\omega_0)=\sin p\omega_0/p\omega_0 \tag{14}$$

The Full line in Fig. 3 shows this correct response function.
If $(p\omega/A)^2$ in (13) is assumed to be negligibly small, we can put $\beta=p\omega$ approximately, and we get

$$R(\omega)=\sin p\omega/p\omega.$$

Thus the contrast of the image of a variable grating becomes the correct response function.

Calculated values of the error

$$\frac{\Delta H}{H}=[R(\omega)-H(\omega_0)]/H(\omega_0) \tag{15}$$

for various k are given in Fig. 4 which affirms that, for measuring $H(\omega_0)$ with the accuracy of 5% when $p\omega_0<2\pi$, a grating of $k<1.15$ should be used. Error in phase of the response function is negligibly small in this case.

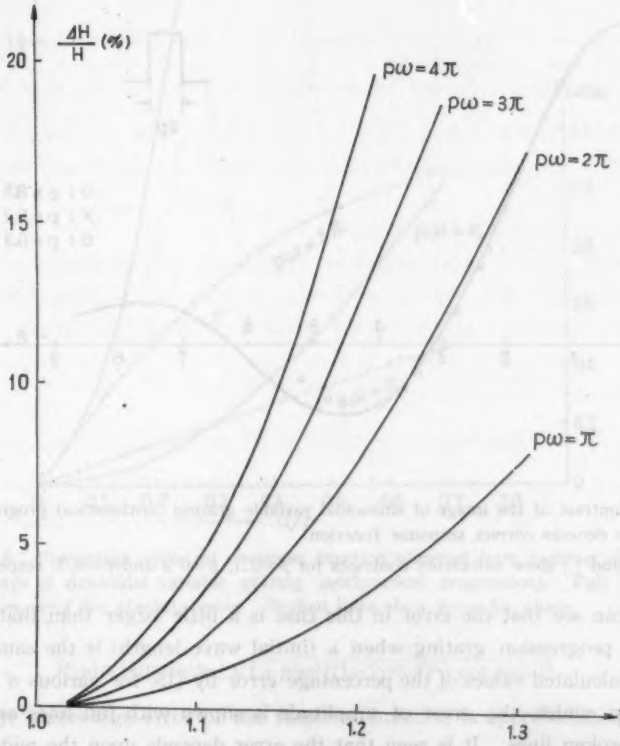

Fig. 4. Percentage error of response function obtained from contrast of the image of sinusoidal variable grating (geometrical progression).

(b) Arithmetical progression grating

The Modulation function of the grating is given by (11) which can however be put in general as

$$f_a(x)=\sqrt{x/\beta}, \qquad \beta=d/8\pi .$$

Intensity distribution of the image in this case is given from (2) as

$$B(y)=\{1+(\beta/p)[g(y+p)-g(y-p)]\}/2$$

where

$$g(t)=\cos\theta+\theta\sin\theta, \qquad \theta=\sqrt{t/\beta}\,.$$

Results of calculation of the contrast therefrom, when $\sqrt{1/\beta}=10\pi$ and $p=0.1$, 0.2, and 0.3, are shown in Fig. 5 with ○, × and □, respectively. In this figure the full line denotes the correct value of the response function (14). Comparing with

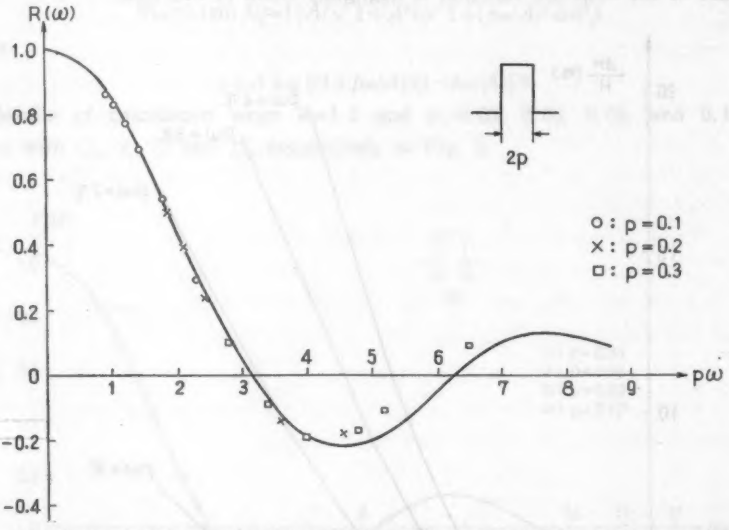

Fig. 5. Contrast of the image of sinusoidal variable grating (arithmetical progression). Full line denotes correct response function.
○, ×, and □ show calculated contrasts for $p=0.1$, $p=0.2$ and $p=0.3$, respectively.

Fig. 3, we can see that the error in this case is a little larger than that with the geometrical progression grating when λ_0 (initial wave length) is the same in both gratings. Calculated values of the percentage error by (15) for various d are given in Fig. 6 in which the error of amplitude is shown with full lines and that of phase with broken lines. It is seen that the error depends upon the width p, and to get the response function as accurate as in the case of geometrical progression grating, a grating of $d/p<0.1$ should be used.

(c) N. B. S.-type grating

In this case the modulation function is given by (8), the integral in (6) is therefore a Fresnel integral and it is hardly possible to find $C(\omega)$ and $S(\omega)$ analytically. But, if we assume $p<y$, it becomes

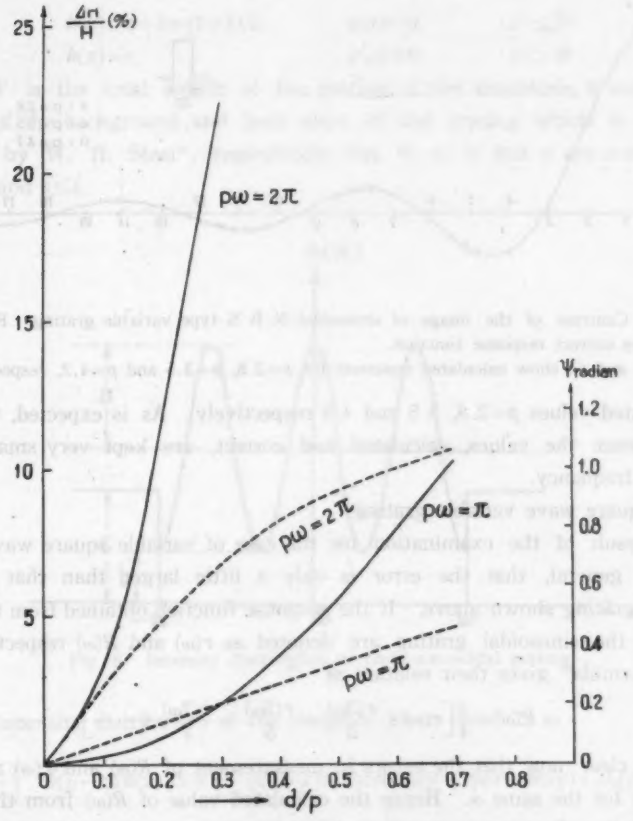

Fig. 6. Percentage error of response function obtained from contrast of the image of sinusoidal variable grating (arithmetical progression). Full lines show error for absolute value. Broken lines show error for phase.

$$R(\omega)=\{\sin p\omega/p\omega\}\sqrt{1+p^4m^2\{(1-2/p^2\omega^2)^2+\cot p\omega/\omega\}^2}.$$

Accordingly, percentage error of the response function is approximately

$$\frac{\Delta H}{H}=p^4m^2/2,$$

except when $p\omega=n\pi$, where n is an integer. As this expression of the error does not contain ω, the response function with constant percentage error up to a very high frequency can be evaluated which is a grate merit of N. B. S.-type grating. In Fig. 7, results of calculation of $R(\omega)$ are shown when $m=\pi/100$. The correct value of the response function is shown by the full line on which ×, △, ○ denote

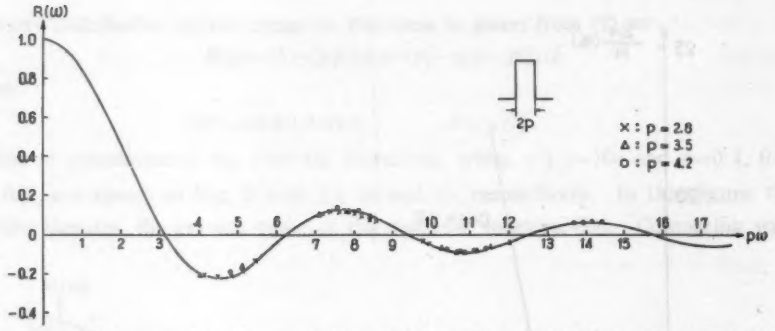

Fig. 7. Contrast of the image of sinusoidal N. B. S.-type variable grating. Full line denotes correct response function.
×, △ and ○ show calculated contrasts for $p=2.8$, $p=3.5$ and $p=4.2$, respectively.

the calculated values $p=2.8$, 3.5 and 4.2 respectively. As is expected, the differences between the values, calculated and correct, are kept very small up to a very high frequency.

(d) Square wave variable grating

The result of the examination for the case of variable square wave grating shows, in general, that the error is only a little larger than that with the sinusoidal grating shown above. If the response function obtained from the square wave and the sinusoidal grating are denoted as $r(\omega)$ and $R(\omega)$ respectively, the Coltman formula[5] gives their relation as

$$R(\omega)=\frac{\pi}{4}\left[r(\omega)+\frac{r(3\omega)}{3}-\frac{r(5\omega)}{5}+\frac{r(7\omega)}{7}+\cdots\right]$$

It became clear now that the errors in measurement of $R(\omega)$ and $r(\omega)$ are of the same order for the same ω. Hence the calculated value of $R(\omega)$ from the experimental results of $r(\omega)$ by the above formula is less accurate than that obtained direct from the sinusoidal grating.

Therefore, a square wave grating with a constant which is smaller than that of a sinusoidal grating has to be used.

Part II. Response function obtained from the image of finite grating

§ 5. General formula

Intensity distribution of a finite grating as is shown in figure 1(B) is given in general as

$$A(x)=k(x)+g(x)\cos\omega_0 x$$

where $k(x)$ is a constant term and $g(x)$ the amplitude modulation function given as

5) J. W. Coltman: J. Opt. Soc. Am. **44** (1954) 468.

$$k(x)=a+b=(1+b)/2, \qquad g(x)=a \qquad |x|\leq W$$
$$k(x)=c, \qquad g(x)=0 \qquad |x|>W$$

where $2W$ is the total length of the grating, a the amplitude, b and c the intensities of the background and both sides of the grating which is called the surround by W. H. Steel[6], respectively (Fig. 8). a, b and c are normalised as $2a+b=1$ and $c\leq 1$.

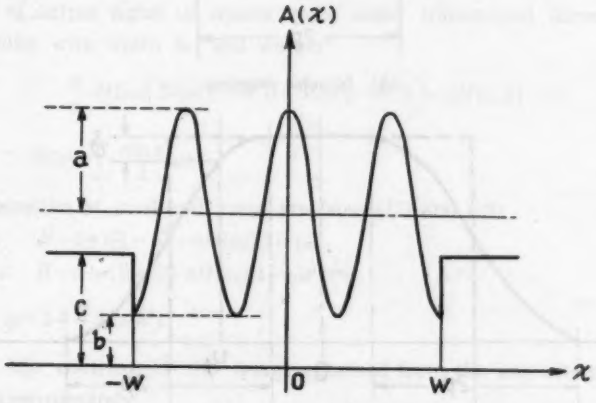

Fig. 8. Intensity distribution of finite sinusoidal grating.

The intensity distribution of the image is given from (2) as

$$B(y)=\int_{-\infty}^{+\infty}k(y-x)\,h(x)\,dx+\int_{-\infty}^{+\infty}g(y-x)h(x)\cos\omega_0(y-x)dx=B_1(y)+B_2(y) \qquad (16)$$

The first term is the image of a single slit with half width W, and can be calculated when the impulse response is given.

The intensities at the points $y=0$ and $y=y_0$ in the image plane are given as shown in Fig. 9(B) as

$$\text{(i)} \quad y=0,\ W\geq p,\ B_1=c\int_{-p}^{p}h(x)dx+\epsilon\int_{-p}^{p}h(x)dx=c+\epsilon=(1+b)/2$$

$$W<p,\ B_1=c+\epsilon(1-\delta_0)$$

$$\text{where} \quad \delta_0=\int_{-p}^{-W}h(x)dx+\int_{W}^{p}h(x)dx \qquad (17)$$

$$\epsilon=\frac{1+b}{2}-c$$

6) W. H. Steel: Optica Acta. **3** (1956) 456.

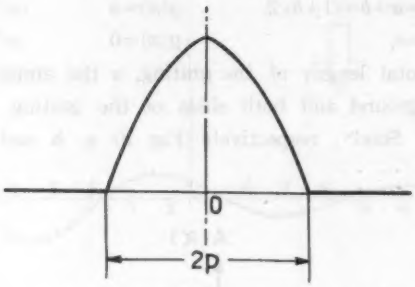

(A) Impulse response

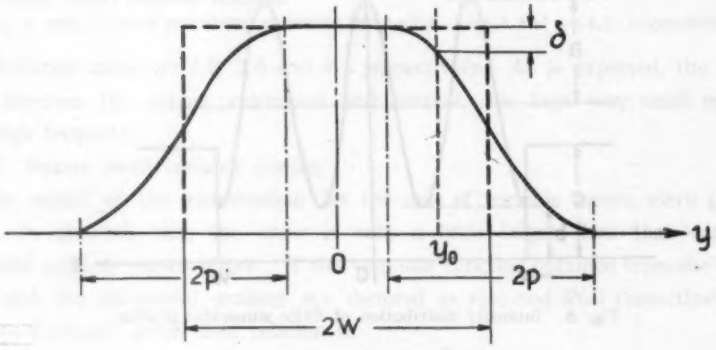

(B) Image of single slit

Fig. 9. Intensity distribution of single slit.

(ii) $y=y_0$ $W\geq p+y_0$ $B_1=c+\epsilon=(1+b)/2$

$W<p+y_0$ $B_1=c+\epsilon(1-\delta)$

where $\delta=\int_{y_0-p}^{-W}h(x)dx+\int_{W}^{y_0+p}h(x)dx$

As to the second term of (16), if we put the Fourier transforms of $h(x)$ and $g(x)$ as $H(\omega_0)$ and $G(u)$, then

$$B_2=a\mathrm{Re}\left[\int_{-\infty}^{\infty}H(\omega_0+u)G(u)e^{iuy}du\right]e^{i\omega_0 y}$$

where *Re* represents the real part of complex quantities.

If W is assumed sufficiently large, u will be limited in a small domain 2α, and $H(\omega_0+u)$ can be expanded into Taylor series as

$$H(\omega_0+u)=H(\omega_0)+u\cdot H'(\omega_0)+\frac{u^2}{2}H''(\omega_0)+\cdots\cdot$$

and the amplitude of B_2 becomes as

$$aH(\omega_0)\int_{-a}^{a} G(u)e^{i\omega_0 u}du+aH'(\omega_0)\int_{-a}^{a} G(u)\cdot u\cdot e^{i\omega_0 u}du\cdots\cdots \tag{18}$$

where $H'(\omega_0)$, $H''(\omega_0)\cdots$are the successive derivatives of $H(\omega_0)$. But, if $H'(\omega_0)$ and a are not so large, some preliminaly calculations showed that the second term has little effect on the result and can be neglected leaving only the first term to be considered.

The first term of (18) is well known in terms of radio communication as the wave form of output signal of square wave input transmitted through an ideal band-pass filter with width $2a$, and we get[7]

$$\frac{a}{\pi}H(\omega_0)\Big[Si(a(y+W))-Si(a(y-W))\Big]=aH(\omega_0)(1-\gamma_l) \tag{19}$$

where $$Si(z)=\int_0^z \frac{\sin z}{z}dz,$$

and the intensities at $y=0$ and $y=y_0$ are from (17) and (19)

$y=0$: $B=c+\epsilon(1-\delta_0)+aH(\omega_0)(1-\gamma_0)$

$y=y_0$: $B=c+\epsilon(1-\delta)+aH(\omega_0)(1-\gamma)e^{i\omega_0 y_0}$

where $$\gamma_0=1-\frac{2}{\pi}Si(aW).$$

Hence, the contrast of the image obtained from the intensities at $y=0$ and $y_0=\pi/\omega$ is approximately

$$R(\omega_0)=\frac{B(0)-B(\pi/\omega)}{B(0)+B(\pi/\omega)}\fallingdotseq H(\omega_0)\left(\frac{1-b}{1+b}\right)\left\{1-\frac{\gamma_0+\gamma}{2}+\frac{\epsilon}{1+b}(\delta_0+\delta)\right\}+\frac{\epsilon}{1+b}(\delta-\delta_0) \tag{20}$$

As is seen from this formula, although $R(\omega_0)$ does not give the correct response function (due to what we shall call the "end effect"), the error $\Delta H(\omega_0)=R(\omega_0)-H(\omega_0)$ is the smaller the larger W, so a grating of a large number of lines should be used to get a better result.

The error also becomes small by selecting a suitable value of ϵ. This is the reason why a grating with gray surround is more effective to reduce the "end effect" than that with black surround[6].

If the attenuation of response function $H(\omega_0)$ is montonous as in the case of an aberrationless ideal optical system, the grating with gray surround of $\epsilon=0$ (that is, if $b=0$, reflection of transmission of the surround is 50%) gives the best result, because in this case γ_0 and γ are very small as compared with δ_0 and δ. However, in the case of a practical optical system with aberrations, γ_0 and γ are not negligibly small; the "end effect" can be reduced by selecting a suitable value of ϵ as shown by the following example.

7) e. g. S. Goldman: Frequency Analysis, Modulation and Noise. (McGraw-Hill, N. Y. (1948) 72.

§6. Numerical example

As an example of the "end effect" given by (20), the case in which the impulse respone is of a square shape as is given by (12) is shown. The contrasts of the finite sinusoidal grating are calculated for the case in which the number of lines are $N=2$, 3, and 4, and $c=0$, 0.3 and 0.5, with $a=0.5$, $b=0$ so $\epsilon=0.5-c$ and $p\alpha=0.35$. The results are plotted by chain lines for $c=0$ (grating with black surround), by dotted lines for $c=0.3$ and by broken lines for $c=0.5$ in Fig. 10.

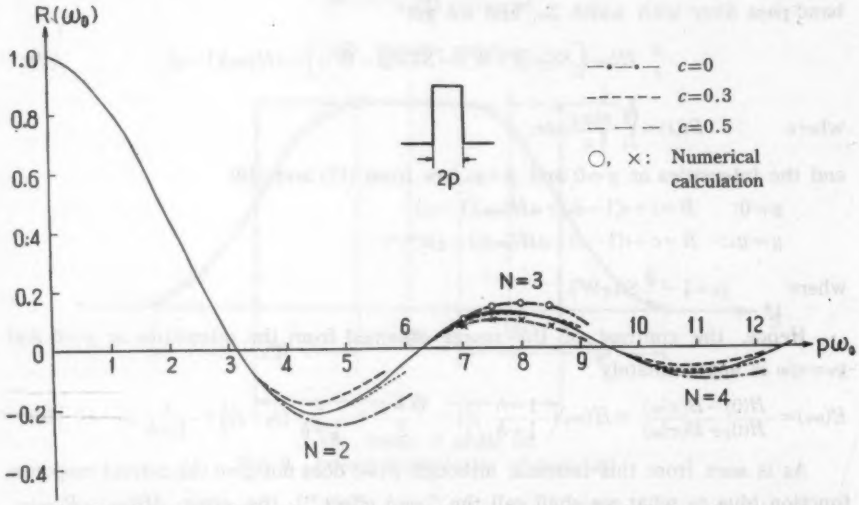

Fig. 10. Contrast of the image of sinusoidal finite grating with 2, 3 and 4 lines for various contrasts of surround. Full line denotes correct response function, chain lines denote calculated contrast for $c=0$, dotted lines for $c=0.3$, broken lines for $c=0.5$

The correct response function of this case is given from (14) and plotted by the full line in the same figure.

If the grating of $c=0.3$ is used, $R(\omega_0)$ becomes nearer to the correct value $H(\omega_0)$ than using either black surround ($c=0$) or gray surround of $c=0.5$. But, it must be remembered that the value of ϵ which gives the best result depends upon the type of the impulse response.

However, we can see from this figure that the results obtained from the contrast of the image are correct in all the cases up to about $(N-1)$th zero of the response function.

Intensity distributions of the image of black and gray surround gratings ($c=0.5$) when $N=3$ are shown in Fig. 11 (A) and (B) for various values of $p\omega_0$.

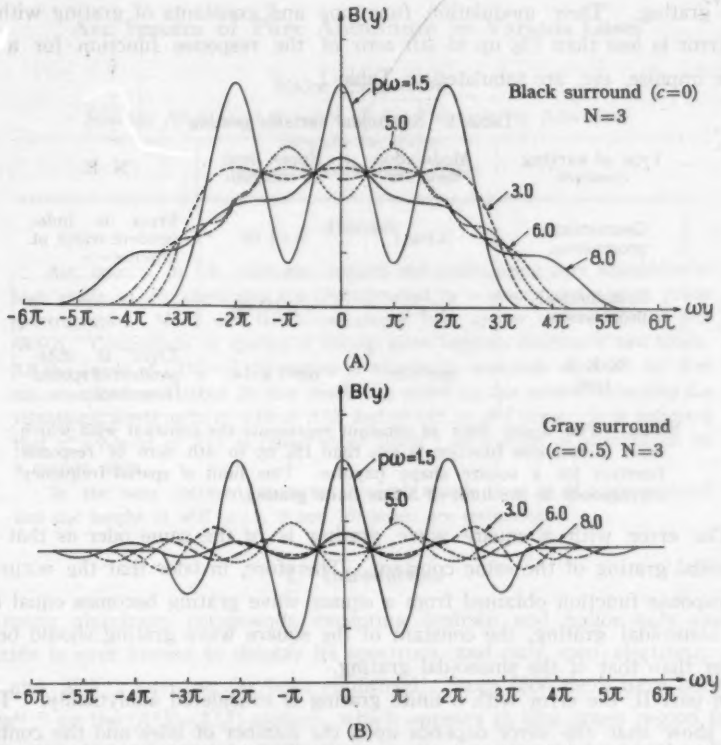

Fig. 11. Intensity distribution of the image of sinusoidal finite grating with 3 lines for various width of impulse response.
(A) in the case of black surround ($c=0$).
(B) in the case of gray surround ($c=0.5$).

The results of calculation of the contrast using the values at $\omega_0 y=0$ and $\omega_0 y=\pi$ in this figure are plotted with ○ and × in Fig. 10. They are in good agreement with the calculated value from (20).

Conclusion

Examination was made if the contrast of the image of "variable grating" and "finite grating" gives the correct response function. As to the case of variable grating, it is shown generally that, when the instantaneous frequency $\frac{df}{dx}=\omega(x)$ is taken as spatial frequency, the contrast of image represents approximately the correct response function. This is confirmed in Part I by numerical calculations with three kinds of sinusoidal gratings, that is, the cases when the pitch varies in geometrical and arithmetical progressions and the case of N. B. S.

type grating. Their modulation functions and constants of grating with which the error is less than 1% up to 4th zero of the response function for a square shape impulse, etc. are tabulated in Table 1.

Table 1. Sinusoidal variable grating

Type of varying constant	Modulation function	Upper limit of constant	N. B.
Geometrical progression	$A \log x$	$k<1.05$	Error is independent width of impulse
Arithmetical progression	$\sqrt{x/\beta}$	$d/p<0.02$	
N. B. S. type	mx^2+lx	$mp^2<0.14$	Error is independent of spatial frequency

NOTE: The upper limit of constant represents the constant with which error of response function is less than 1% up to 4th zero of response function for a square shape impulse. This limit of spatial frequency corresponds to the limit of 5 line finite grating.

The error with a square wave grating is of the same oder as that with a sinusoidal grating of the same constant. Therefore, in oder that the accuracy of the response function obtained from a square wave grating becomes equal to that of a sinusoidal grating, the constant of the square wave grating should be much smaller than that of the sinusoidal grating.

In part II, the error with a finite grating is considered analytically. The results show that the error depends upon the number of lines and the contrast of the grating. If the grating has N lines, the correct response function will be obtained up to the $(N-1)$th zero of the response function for a square shape impulse. It is also shown that the gray surround is more profitable than the black surround.

When the so called "Siemens' Star" is used as the chart for measuring the response function, there also occur errors of the same kind due to the continuous change of the grating constant along the radius of the star. As to the error in this case we have an excellent computation by K. P. Miyake[8].

Acknowledgment

The author wishes to express his thanks to Dr. H. Kubota of the University of Tokyo for his helpful suggestion and criticism in the course of this study. He also greatly indebted to Miss. Tsuneko Suzuki who performed most part of the numerical computation involved in this work.

8) K. P. Miyake: Science of Light. **7** (1958) 9.

Arc Spectra of Pure Aluminum in Various Gases

Midori SHIMAUCHI

Institute for Optical Research, Tokyo University of Education, Shinjuku-ku, Tokyo

(Received December 1, 1958)

Abstract

Arc spectra in air, nitrogen, oxygen and argon using pure aluminum of high grade as two electrodes are photographed by a quartz and a glass prism spectrographs. Many new bands and atomic lines appear between 2500 A and 8800 A. Comparison of spectra in various gases suggests emitters of new bands. All the heads of $(A^2\Sigma-X^2\Sigma)$ system of aluminum monoxide reported by Roy are examined and about 20 new heads are added to this system extending the vibrational levels up to $v''=12$ of $X^2\Sigma$ and $v'=16$ of $A^2\Sigma$ state. It is indicated that $v''=9$ level of $X^2\Sigma$ is raised about 10 cm^{-1} on account of perturbation by a certain state.

In the near infrared spectrum several atomic lines of Al I are analyzed and the height of n^2F ($n=8$, 9 and 10) levels are estimated.

1. Introduction

Among aluminum compounds excepting hydride and halide only aluminum monoxide is ever known to display its spectrum, and only two electronic states, $A^2\Sigma^+$ and $X^2\Sigma^+$, have so far been confirmed. Since 1866 there have been many reports[1)-5)] on the $(A^2\Sigma-X^2\Sigma)$ system, which appears in blue-green region forming clear groups of heads, and in 1925[6)] their emitter was proved to be the diatomic oxide molecule, AlO. In 1939 D. Roy[5)] made precise measurements of the heads of this system including many new ones between 4150–5700 A. As the result of his analysis the vibrational levels of $A^2\Sigma$ and $X^2\Sigma$ state have been extended respectively to $v'=14$ and $v''=11$.

Later the predissociation in the (0—0) band of this system at $K=129$ was observed by Coheur-Dehalu[7)], which was supported by B. Rosen[8)]. Rosen proposed the predissociation in the lower $^2\Sigma$ state on account of perturbation by a certain repulsive state, and concluded that all the bands with $v''\geq 9$ are predissociated.

1) R. Mecke: Phys. Zeit. **26** (1925) 217.
2) G. Eriksson and E. Hultén: Z. Phys. **34** (1925) 775.
3) W. C. Pomeroy: Phys. Rev. **29** (1927) 59.
4) M. K. Sen: Indian J. Phys. **11** (1937) 251.
5) D. Roy: Indian J. Phys. **13** (1939) 231.
6) R. Mulliken: Phys. Rev. **26** (1925) 561.
7) F. Coheur-Dehalu: Bull. Acad. Roy. Belgium **23** (1937) 604.
8) B. Rosen: Phys. Rev. **68** (1945) 124.

From this proposition it follows that one of the two atoms resulting from the dissociation of AlO in $X^2\Sigma$ state must be in excited state; the products of the dissociation are probably $Al(^2P)$ and $O(^1D)$. And according to this view, the dissociation energy should be as low as 0.93 eV. Recently, however, Lagerqvist, Nilssson and Barrow[9], after examining the (0-0) band of the $(A^2\Sigma-X^2\Sigma)$ system with a high resolving power spectrograph, stated that the observed predissociation at $P(129)$ is really an instrumental effect and that all the other reported predissociations in this system might have been illusory.

As regards other systems of aluminum monoxide, F. P. Coheur and B. Rosen published a report in 1941[10]. Using the exploding wire technique, they found many heads in the region of 2500−3500 A and tried to analyze them. In their result there is $(B-X^2\Sigma)$ system[11] and a reasonable Deslandres table with 28 heads was formed. However it seems desirable to examine this system further because the heights of vibrational levels of lower state with $v''\geq 5$ are lower than those obtained from $(A^2\Sigma-X^2\Sigma)$ system.

It is also interesting to search for a $^2\Pi$ state corresponding to $A^2\Pi_i$ state of BO and for this purpose an investigation in the near infra-red seems necessary. Moreover the spectra of other aluminum compounds such as AlN and AlS are interesting from the point of view of molecular structure. It seems also worthwhile searching for the spectrum of Al_2 because that of B_2 has already been investigated[12].

Spurred by this interest the author sought the methods of exciting aluminum compounds. The arc between pure aluminum electrodes in various gases appears fairly useful for this purpose. The arc in air in this method displayed the spectra of many bands in the region of 2500−3500 A, and $(A^2\Sigma-X^2\Sigma)$ system of AlO was extended to 4050 A revealing one more sequence than has ever been reported. The arc spectra in nitrogen, oxygen and argon with pure aluminum electrodes were photographed, and some of the new heads and atomic lines appearing in them were analyzed.

2. Experiments

The arc was run from D. C. 100 V supply through a resistance of 20 ohms. Pure aluminum of high grade was employed as the two electrodes in order to avoid the spectrum of any impurity. The aluminum was graded 99.994% pure with Fe, Cu and Si as impurities, each of which being less than 0.002% with just

9) A. Lagerqvist, N. E. Lennart Nilsson and R. F. Barrow: Proc. Phys. Soc. **69** (1956) 356.
10) F. P. Coheur and B. Rosen: Mem. Soc. Roy. Sci. Liége (1941) 405.
11) G. Herzberg: *Spectra of Diatomic Moleules* (1950) p. 504 (Van Nostrant Comp., New York).
12) A. E. Douglas and G. Herzberg: Canad. J. Res. **A 18** (1940) 165.

a trace of Mn. Several shapes of electrodes were tried in search for the best to prolong the arcing and at the same time to facilitate the display of spectra of many bands. A rod of 10 mm in diameter as the lower negative electrode and a rolled foil of 0.1 mm in thickness or two or three wires of 1 mm in diameter twisted together as the upper electrode were found fairly satisfactory for the purpose. It was necessary to keep the electrodes free from oil or fat, for aluminum seemed to adsorb them very easily on its surface causing strong CN bands to appear impeding the observation. The discharge tube was made from two liter flask and one of the electrodes was operated by a bellows.

The pressure of gas was kept at almost 760 mmHg, for in low pressures, gas appeared easily excited to show its spectrum. The employed gases were nitrogen and argon of high grade and commercial oxygen in bomb. Nitrogen was further purified by passing it through heated copper flinders to remove even a trace of oxygen to avoid the other spectra being obscured by the blue-green system of AlO. Arc in purified nitrogen or argon never goes out provided the distance between the electrodes is properly kept. But, since arc in oxygen dies out in no time, photographing of the spectrum of AlO was made with arc in air. The following seemed worth remembering for the analysis of the result: both electrodes and walls of the discharge tube were whitened with aluminum oxide (Al_2O_3) powder when even a trace of oxygen existed in the discharge tube; they were coloured grayish black with aluminum nitride (AlN) powder when purified nitrogen was used; they remained clean in argon.

The spectra in visible and near infra-red regions were photographed by a glass spectrograph composed of three 60° prisms of 6 cm base and a camera lens of 50 cm focal length. The dispersion was about 46 A/mm at 6000 A. For ultra-violet region a Hilger E_1 quartz spectrograph was used. The photographic plates employed were Fuji process and Neopan Type for ultra-violet and visible regions respectively, Kodak I-N for near infra-red region.

Iron arc lines were taken as reference standards through the whole region. The probable error in wavelength determination was about ±0.1 A in the range observable with E_1 spectrograph, ±0.3 A in the visible region. But it amounted to ±1.2 A in the near infra-red region.

3. Results and Discussion

(1) Visible and near ultra-violet region

This is the region where ($A^2\Sigma - X^2\Sigma$) system of AlO dominates. The arc spectrum in air showed almost twenty new heads. Removal of disturbing Fe atomic lines and heads of CN violet system enabled a new sequence of $\Delta v = 5$ between

Table 1. Deslandres table of $(A^2\Sigma - X^2\Sigma)$ system of AlO

v′ \ v″	0		1		2		3		4		5	
0	4842.18 (10) 20646.1	964.1	5079.37 (9) 19682.0	950.2	5337.03 (4) 18731.8	930.1	5615.88 (0) 17801.7					
	862.2		862.0		862.9		857.7					
1	4648.08 (8) 21508.3	964.3	4866.23 (8) 20544.0	949.3	5102.01 (10) 19594.7	935.3	5357.75 (6) 18659.4	920.0	5635.60 (1) 17739.4			
	854.9		854.4		854.4		854.6		853.4			
2	4470.38 (6) 22363.2	964.8	4671.94 (8) 21398.4	949.3	4888.83 (6) 20449.1	935.1	5123.08 (10) 19514.0	921.2	5376.93 (6) 18592.8	905.5	5652.21 (1) 17687.3	
	847.2		848.2		846.9		846.8		847.2		845.7	
3	4307.21 (3) 23210.4	963.8	4493.82 (7) 22246.6	950.6	4694.40 (8) 21296.0	935.2	4910.02 (0) 20360.8	920.8	5142.60 (10) 19440.0	907.0	5394.27 (6) 18533.0	890.7
	839.8		839.5		840.1		839.9				839.1	
4	4156.80 (2) 24050.2	964.1	4330.39 (4) 23086.1	950.0	4516.24 (7) 22136.1	935.4	4715.50 (8) 21200.7				5160.62 (10) 19372.1	892.0
			831.9		832.0		831.4					
5			4179.78 (2) 23918.0	949.9	4352.64 (4) 22968.1	936.0	4537.57 (7) 22032.1	922.8	4735.92 (7) 21109.3			
			820.2		824.5		825.0		826.7			
6			**4041.2 (0) 24738.2**	**945.6**	4201.81 (3) 23792.6	935.5	4373.78 (4) 22857.1	921.1	4557.44 (7) 21936.0	907.1	4754.04 (6) 21028.9	
					816.5		816.9		816.8		816.9	
7					**4062.4 (0) 24609.1**	**935.1**	4222.85 (3) 23674.0	921.2	4393.84 (5) 22752.8	907.0	4576.26 (6) 21845.8	892.8
							812.7		809.1		810.3	
8							**4082.7 (0) 24486.7**	**924.8**	4242.94 (3) 23561.9	905.8	4412.58 (5) 22656.1	893.9
									806.0		800.3	
9									**4102.6 (0) 24367.9**	**911.5**	4262.03 (3) 23456.4	890.9
											799·2	
10											**4121.6 (1) 24255.6**	**897.9**
11												
12												
13												
14												
15												
16												

The values in Gothic are new, and those marked with * are revised.

6		7		8		9		10		11		12
5666.62 (2) 17642.3												
837.8												
5409.73 (6) 18480.1	877.6	5679.45 (1d) 17602.5										
831.7		833.4										
5176.75 (9) 19311.8	875.9	5422.70 (6) 18435.9	866.7	5690.20 (0d) 17569.2								
		821.2		826.2								
		5191.44 (9) 19257.1	861.7	5434.64 (4) 18395.4	862.0*	5701.8* (0d) 17533.4						
				814.3		820.2						
4771.26 (5) 20953.0				5204.25 (7) 19209.7	856.1*	5447.0* (5) 18353.6	(828.2)*	(5704.41) (17525.4)				
809.2				**808.0**		805.7*		(806.3)				
4593.85 (5) 21762.2	878.6	4787.10 (4) 20883.6	**865.9**	**4994.2 (0) 20017.7**	**858.4**	5218.0* (3) 19159.3	827.6*	5453.52 (5) 18331.7	(819.7)	(5708.80) (17512.0)		
803.3		802.0		**805.8**		**799.2**				(801.5)		
4430.31 (5) 22565.5	879.9	4610.07 (5) 21685.6	862.1	4800.92 (2) 20823.5	**865.0**	**5009.0 (0) 19958.5**				5458.94 (4) 18313.5		
792.2		794.8		791.1								
4280.05 (3) 23357.7	877.3	4447.08 (5) 22480.4	865.8	4625.20 (5) 21614.6		not clear in our spectrum		**5016.9 (0) 19927.1**				**5464.0 (4d) 18296.5**
792.4		788.2		788.9								
4139.6 (1) 24150.1	**881.5**	4296.44 (3) 23268.6	865.1	4462.33 (4) 22403.5	861.0*	4640.7* (4d) 21542.5				**5024.4 (1) 19897.3**		
				783.8*		782.5						
		in the shade of (4–0)		4311.5* (3) 23187.3	863.1*	4478.2* (4d) 22324.2	(826.2)*	(4650.30) (21498.0)				**5032.6 (0) 19864.9**
				774.7				(765.6)				
				4172.1 (2) 23962.0		**overlap with (4–1)**		4490.38 (3) 22263.6	**823.3**	**4662.8 (1) 21440.3**		
								766.1		**764.2**		
						4190.8 (2) 23855.1	**825.4**	**4341.0 (2) 23029.7**	**825.2**	4502.34 (2) 22204.5		
								in the shade of (6–2)		**in the shade of (5–2)**		**4512.3 (1) 22155.5**
												750.2
										4216.5 (2) 23709.6	**803.9**	**4364.5 (2d) 22905.7**

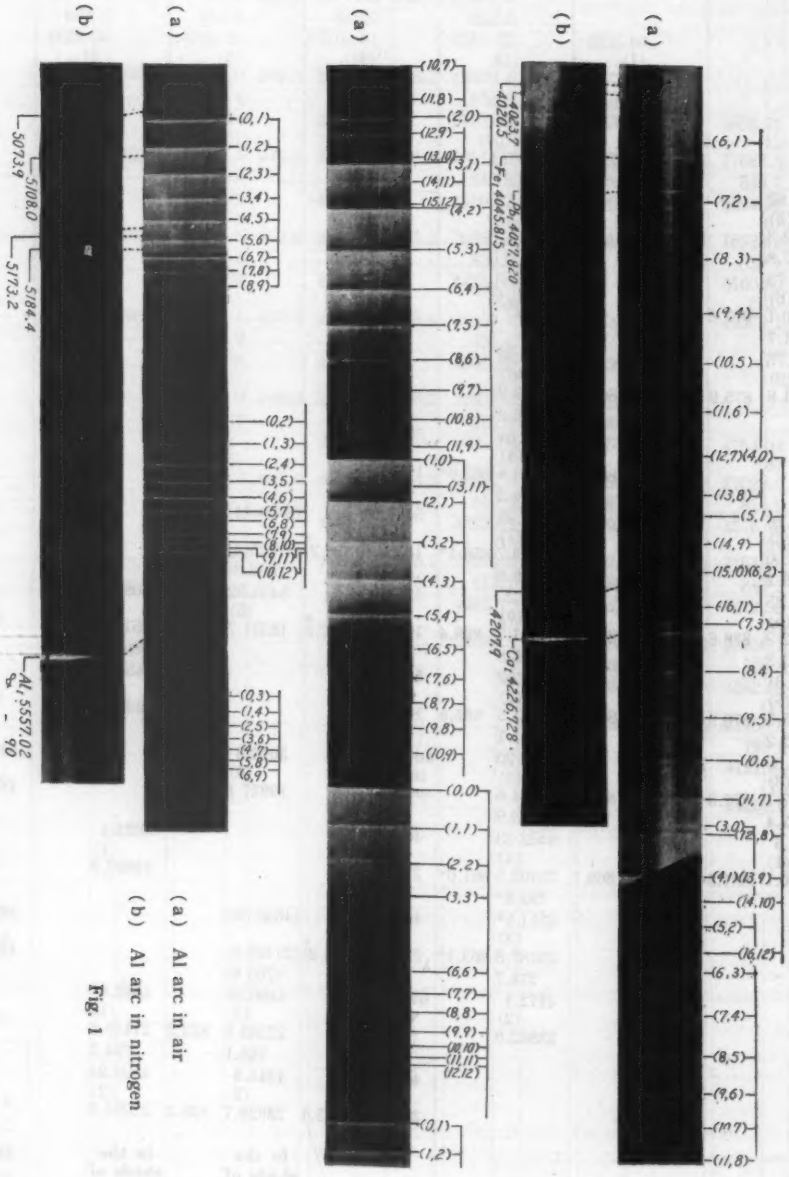

(a) Al arc in air

(b) Al arc in nitrogen

Fig. 1

4041 A and 4217 A to appear. In this sequence the bands with high vibrational quantum numbers have fairly strong intensities and the band of (16−11) is clearly observed. The result of analysis is shown in Table 1, in which the newly found heads are in Gothic and numbers in brackets are the estimated intensities. All the heads reported by D. Roy[5] were examined, and the wavelengths of those heads with which the present result agree within experimental error are given in Roy's figures without any sign, for his measurements appeared more precise than the author's on account of better spectrograph. The values which could not be exmined are in parentheses. At the wavelengths, 5445.05 A, 5216.20 A and 4476.02 A, which were reported by Roy[5] as the positions of heads of (7−9), (8−9) and (12−9) bands respectively, no such indication was found. However about 2 A on the longer side of each of them there are what are to be regarded as heads. The average difference of wavenumbers between Roy's and the author's is about 10 cm^{-1}, which far exceeds the experimental error. Similarly what exists at 4638.77 A that is reported by him as the head of (11−9) band looks hardly acceptable as a head, and what exists slightly (1.9 A) on the longer side of it appears more like a head. Therefore the revised values are listed in Deslandres table with asterisks. Taking acount of all the revision and the positions of new bands with $v''=9$, it is concluded that the vibrational level of $v''=9$ of $X^2\Sigma$ state is perturbed and raised about 10 cm^{-1} by a certain state. All the heads of bands with $v''=9$ seem a little more diffuse than the others. The analysis of the vibrational levels was extended up to $v''=12$ of $X^2\Sigma$ state, but no appreciable perturbation to the levels of $v''=10$, 11 and 12 was found, for the calculated wavenumbers using Roy's foamula agree with those observed within the experimental error. It should be noted that the head of (12−8) band does not appear at the reported position[5], and the revised value is listed also with an asterisk.

At the tail of $\Delta v=0$ sequence, some heads seem to overlap some rotational lines, and the positions of abnormaly strong lines coincide with the calculated values of heads of (8−8), (9−9), (10−10), (11−11) and (12−12) bands. The apperance of these bands seems reasonable, for they might probably represent subsidary intensity maxima on Deslandres table.

The arc in nitrogen or in argon shows no band spectrum in this region. Atomic lines of aluminum are easily excited in the arc in nitrogen, and several new lines appear when pure aluminum of high grade is employed as electrodes. Although they are not capable of being combined with the known atomic energy levels of Al I[13], they might possibly be the atomic lines of Al I, since no line of

13) C. E. Moore: *Atomic Energy Levels* I, (1949) p. 124-143 (Circular of National Bureau of Standards 467, Washington).

Al II[14),15),16)] or Al III[15),16)] appeared over the whole region investigated. For reference, some values of them are listed in Table 2, and their photographs are shown in Fig. 1, in which the arc spectra in air and in nitrogen are placed side by side.

Table 2. Unanalyzed lines of Al

λ	Int.	ν	Reference
4020.5	2	24865.5	*
4023,7	2	24845.7	*
4207.9	1	23758.1	*
5073.9	4 d	19703.2	
5108.0	3 d	19571.7	slightly shades towards red
5173.2	3	19325.0	
5184.4	4	19283.3	
5588.7	1	17888.3	*
5594.1	0	17871.0	*
6122.6	1	16328.4	
6162.6	2	16222.4	
6440.8	1	15521.7	
6464.4	1	15465.1	

All the lines listed are observed most clearly in the arc spectrum in nitrogen, while those marked with * appear sometimes in the arc in air.

(2) Near infra-red region

In this region, the spectrum in air or in oxygen is obscured by a continuous spectrum, whereas that in nitrogen is most interesting. In this spectrum no atomic line of nitrogen appears, while in the arc in argon atomic lines of argon are easily excited. In Fig. 2 the arc spectra in nitrogen and argon are shown side by side for the convienience of comparison. In the arc in nitrogen the diffuse (4^2P-n^2D) and the sharp (4^2D-n^2S) series, which have been observed only in some specific discharges[14),15),16)], appeared clearly with more intensity than in the discharge. Three new lines listed in Table 3 are readily analyzed as the extension of these series. Their wavelengths estimated from "Atomic Energy Levels[13)]" are in accord with those observed. The lines of fundamental (3^2D-n^2F) series appear strongly with shade about forty to seventy cm^{-1} towards red in the arc spectrum in nitrogen, while they have no shade when the atmosphare of arc is argon. This series was extended up to $n=10$. The observed wavelengths of lines and

14) F. Paschen and R. Ritschl: Ann. Phys. [Leibzig] (**5**) **18** (1933) 886.
15) G. R. Harrison: *M. I. T. Wavelength Tables* (1939) (John Willey and Sons, Inc., New York)
16) *Spectraltabellen* (1955) (Veb Verlag Technik, Berlin).

(a) Al arc in argon
(b) Al arc in nitrogen

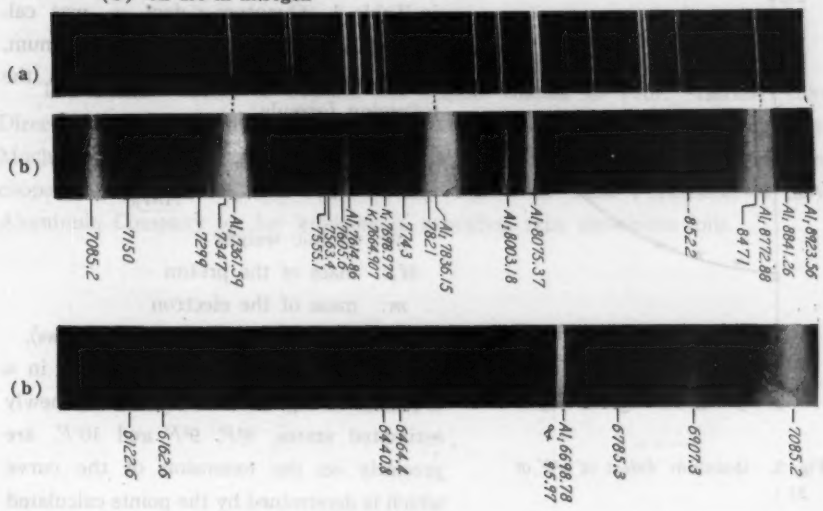

Fig. 2

Table 3. Analyzed lines of Al I

λ_{obs}	Int.	λ_{cal}	ν_{cal}	Transition
7605.6	3	7605.3	13144.06	$(4^2P_{3/2}-8^2D_{1/2})$
7563.4	2	7562.9	13218.83	$(4^2P_{3/2}-9^2S_{1/2})$
7555.1	1	7553.8	13234.66	$(4^2P_{1/2}-9^2S_{1/2})$

Table 4. n^2F Rydberg Series of Al I

n	λ_{obs}	Int.	ν_{obs}	height of n^2F	quantum defect, μ
4				41318.74*	0.029
5	(8772.88)	10	(11395.63)		
	8773.1		11395.4	43831.08*	0.033
6	(7835.33)	9	(12759.20)		
	7835.3		12759.2	45194.65*	0.035
7	(7361.59)	8	(13580.27)		
	7362.8		13578.9	46015.73*	0.037
8	7085.2	5	14110.4	46545.85	0.043
9	6907.3	3	14473.5	46908.95	0.051
10	6785.3	1	14733.7	47169.15	0.056

The values in brackets are taken from the report of Paschen and Ritschl[14], and those marked with * from "Atomic Energy Levels"[13].

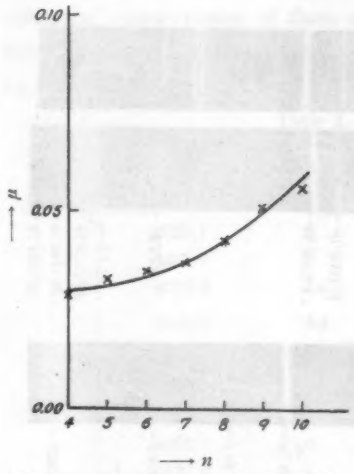

Fig. 3. Quantum defect of n^2F of Al I.

estimated heights of n^2F levels are listed in Table 4. Quantum defect, μ, was calculated using Rydberg constant of aluminum, 109735 cm^{-1}, which was obtained from the following formula:

$$R_A = \frac{R_\infty}{1+\frac{m}{AM_p}}$$

A: atomic weight
M_p: mass of the proton
m: mass of the electron
R_∞: Rydberg constant (infinite mass).

The variation of μ with the increase in n is plotted in Fig. 3. The μ values of newly estimated states, 8^2F, 9^2F and 10^2F, are precisely on the extension of the curve which is determined by the points calculated from the heights of already known states, 4^2F, 5^2F, 6^2F and 7^2F[13].

There are several new heads of bands, whose shades, wavelengths and wavenumbers are, for reference, listed in Table 5. It is possible that these bands are emitted from aluminum nitride or aluminum molecule, since they appear clearly when purified nitrogen is used as the ambient gas, while even the strongest head of $(A^2\Sigma - X^2\Sigma)$ system of AlO does not appear. The arc in argon reveals no bands.

Some of the heads observed between 2500 A and 3500 A coincide with those reported by F. P. Coheur and B. Rosen[10]. They are certainly emitted from oxide of aluminum, because they appear in the arc spectrum in air or in oxygen and

Table 5. Heads appearing in the arc spectrum in pure N_2.

λ_{obs} A	Int.	ν_{obs} cm^{-1}	reference
8741	8	11437	violet shade, overlaid by Mn I 8740.93
8522	3	11731	violet shade
7821	8	12783	red shade
7806	3	12808	red shade
7743	5	12911	violet shade
7347	3	13607	red shade
7299	3	13696	red shade
7150	1	13982	violet shade
7040	1	14201	red shade

not in pure nitrogen. However they are left unanalysed; overlapping of many bands made the analysis difficult.

Acknowledgement

The author wishes to express her sincere thanks to Prof. Haruo Ôtuka, Director of the Institute for Optical Research, for his interest and encouragement. Much appreciation is also due to Prof. Masao Seya for his valuable advice and cooporation throughout this work. Many thanks to Miss Furushima at Tôyô Aluminum Company for her kindness in providing pure aluminum foils.

On the Relation Between Tristimulus Values of Color and Color Temperatnre of Planckian Radiation

Miyoshi HARADOME

Department of Applide Physics, Faculty of Engineering University of Tokyo, Japan

(Received December 1, 1958)

Aastract

Approximate relations between C. I. E. tristimulus values (X, Y and Z) of color and colar temperature (T) of Planckian radiation are investgated with numerous colors. Following relations are found.

$$X=a_x+b_x(1/T\times10^6)+C_x(1/T\times10^6)^2$$
$$Y=a_y+b_y(1/T\times10^6)+C_y(1/T\times10^6)^2 \qquad \text{when } T\simeq3000\sim7000°\text{K}$$
$$Z=a_z+b_z(1/T\times10^6)+C_z(1/T\times10^6)^2$$

For these empirical equations, some theoretical considerations are made.

These quadratic forms can be used in the calculation of tristimulus values of color of Planckian radiation at any color temperature.

1. Introduction

Color stimulus values of an object are changed when color temperature of the illuminating light is changed. For example, even if the tristimulus values of two objects are equal under irradition at a certain color temperature, they may

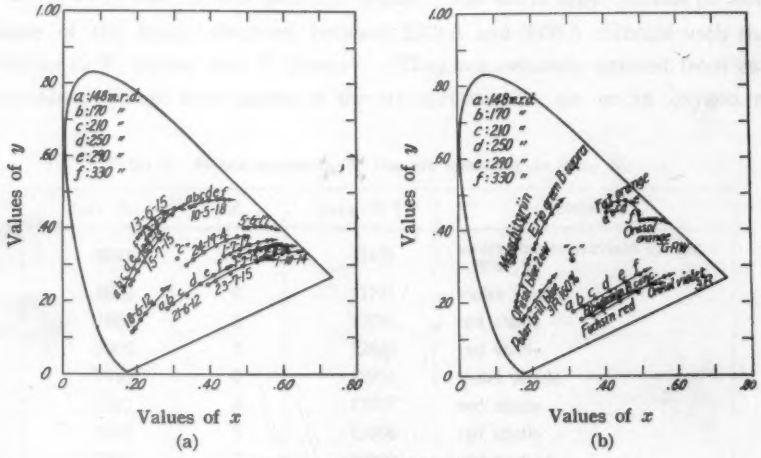

Fig. 1. Chromaticity diagram.

be different under irradiation at other color temperatures*.

Thus, as shown in Figs. 1a and 1b, various colors have various loci with the change of color temperature of the illuminating light, which is proved in actual cases. For example, although an object is colored under a certain standard light to have the same color stimulus values as those of a given sample and is color-matched, if the color temperature of the light is altered, the colors may no longer match.

The relation of tristimulus values of color to the color temperature of illuminating light was studied and empirical formulas which would be useful for practical calculations are presented in this work.

2. Theroretical consideration

2.1. Tristimulus values of light source color.

Tristimulus values of light source color are defined by

$$L=\int_V^R E_\lambda \cdot \bar{S}_\lambda \cdot \rho_\lambda d\lambda \tag{1}$$

where E_λ is the radiation energy of the black body given by Placck's formula and can be expanded as follows.

$$E_\lambda = C_1/\lambda^5 \cdot \frac{1}{\exp[C_2/\lambda T]-1} = (C_1 T/C_2\lambda^4)\left[1+\frac{C_2/\lambda T}{2!}+\frac{(C_2/\lambda T)^2}{3!}+\cdots\cdots\right]^{-1}$$

$$= C_1/C_2 \cdot T/\lambda^4\left[1-\frac{1}{2}\cdot\frac{C_2}{\lambda T}+\frac{1}{12}\left(\frac{C_2}{\lambda T}\right)^2-\frac{1}{720}\left(\frac{C_2}{\lambda T}\right)^4+\cdots\cdots\right] \tag{2}$$

$\bar{S}_\lambda$ is an approximate function for tristimulus values of equi-enengy spectrum that are distribution coefficients ($\bar{x}$, $\bar{y}$, $\bar{z}$). Peason's distribution function is used for $\bar{S}_\lambda$, which is defined by

$$\bar{S}_\lambda = A/\lambda^P \cdot \exp[-q/\lambda] \tag{3}$$

where λ is the wave-length, A, P and q are constants.

ρ_λ in (1) is the spectral characteristic of color and can be expressed by a power series expansion of spectral reflection or transmission curve as

$$\rho_\lambda = \sum_{m=0}^{\infty} B_m \lambda^m \tag{4}$$

therefore, from (1), (2), (3) and (4), we obtain

$$L=\int_B^R E_\lambda \cdot \bar{S}_\lambda \cdot \rho_\lambda d\lambda = AC_1\left(\frac{T}{C_2}\right)\sum_{m=0}^{\infty}\left[\int_0^\infty B_m \cdot \lambda^m/\lambda^{P+4} \cdot e^{-q/\lambda}d_\lambda - \frac{1}{2}\left(\frac{C_2}{T}\right)\int_0^\infty B_m \cdot \lambda^m/\lambda^{P+5} \cdot e^{-q/\lambda}d\lambda\right.$$

* In this discussion, the light source is assumed to have the spectral energy distribution approximtely equal to that of the black body.

$$+\frac{1}{12}\left(\frac{C_2}{T}\right)^2\int_0^\infty B_m\cdot\lambda^m/\lambda^{P+6}\cdot e^{-q/\lambda}d\lambda-\frac{1}{720}\left(\frac{C_2}{T}\right)^4\int_0^\infty B_m\cdot\lambda^m/\lambda^{P+7}\cdot e^{-q/\lambda}d\lambda+\cdots\cdots\Big] \quad (5)$$

putting $1/\lambda=x$

$$L=AC_1\left(\frac{T}{C_2}\right)\sum_{m=0}^{\infty}\Big[\int_0^\infty B_m\cdot x^{P-m+2}\cdot e^{-q\cdot x}dx-\frac{1}{2}\left(\frac{C_2}{T}\right)\int_0^\infty B_m\cdot x^{P-m+3}\cdot e^{-q\cdot x}dx$$

$$+\frac{1}{12}\left(\frac{C_2}{T}\right)^2\int_0^\infty B_m\cdot x^{P-m+4}\cdot e^{-q\cdot x}dx-\frac{1}{720}\left(\frac{C_2}{T}\right)^4\int_0^\infty B_m\cdot x^{P-m+5}\cdot e^{-q\cdot x}dx+\cdots\cdots\Big]$$

$$=\sum_{m=0}^{\infty}A\cdot B_m\cdot C_1\left(\frac{T}{C_2}\right)\Big[\frac{\Gamma(P-m+3)}{q^{P-m+3}}-\frac{1}{2}\left(\frac{C_2}{T}\right)$$

$$\times\frac{\Gamma(P-m+4)}{q^{P-m+4}}+\frac{1}{12}\left(\frac{C_2}{T}\right)^2\frac{\Gamma(P-m+5)}{q^{P-m+5}}-\frac{1}{720}\left(\frac{C_2}{T}\right)^4\frac{\Gamma(P-m+6)}{q^{P-m+6}}+\cdots\cdots\Big]$$

$$=\sum_{m=0}^{\infty}A\cdot B_m\cdot C_1\cdot\frac{\Gamma(P-m+3)}{q^{P-m+3}}\cdot\left(\frac{T}{C_2}\right)\Big[1-\frac{1}{2}\left(\frac{C_2}{T}\right)\frac{(P-m+3)}{q}+\frac{1}{12}\left(\frac{C_2}{T}\right)^2$$

$$\times\frac{(P-m+3)(P-m+4)}{q^2}-\frac{1}{720}\left(\frac{C_2}{T}\right)^4\frac{(P-m+3)(P-m+4)(P-m+5)(P-m+6)}{q^4}$$

$$+\frac{1}{30240}\left(\frac{C_2}{T}\right)^6\frac{(P-m+3)\cdots(P-m+8)}{q^6}$$

$$-\frac{1}{1209600}\left(\frac{C_2}{T}\right)^8\frac{(P-m+3)\cdots(P-m+10)}{q^8}\Big] \quad (6)$$

The constants P and q in (3) are given by P. Moon and D. E. Spencer[1),2)] as shown in Table 1. As seen in this table, any set of P and q can be used as the approximate values of spectral distribution coefficients within a particular spectral region. Accordingly the whole spectral region is divided into several intervals.

Table 1 Values of the constants in Eq (3)

$\bar{x}_{(\lambda)}=\bar{x}_{A(\lambda)}-\bar{x}_{B(\lambda)}+\bar{x}_{C(\lambda)}:\bar{x}_{A(\lambda)}=\bar{z}_{(\lambda)}/4.570$
$\bar{y}_{(\lambda)}=\bar{y}_{A(\lambda)}$, $\lambda\leqq0.620\,\mu:\bar{y}_{A(\lambda)}-\bar{y}_{B(\lambda)}$, $0.620\leqq\lambda\leqq0.670\,\mu$, $\bar{y}_{(\lambda)}=\bar{y}_{C(\lambda)}$, $\lambda\leqq0.670\,\mu$

	$\bar{z}_{(\lambda)}$	$\bar{x}_{B(\lambda)}$	$\bar{x}_{C(\lambda)}$	$\bar{y}_{A(\lambda)}$	$\bar{y}_{B(\lambda)}$	$\bar{y}_{C(\lambda)}$
P	365.3388	500.0000	336.0385	182.1905	3.2050	1013.50
q	164.9506	237.5000	199.1054	100.9370	0.12820	679.045

Let us use just one appropriate set of P and q in the following discussion.

Now, assuming $P-m>180$ and $T=3000\sim7000$°K (6) can be written approximately as follows.

1) J. Opt. Soc. Amer., **33**, 89–103 (1943).
2) J. Opt. Soc. Amer., **35**, 399–427 (1945).

$$L\fallingdotseq\sum_{m=0}^{\infty}A\cdot B_m\cdot C_1\frac{\Gamma(P-m+3)}{q^{P-m+3}}\left(\frac{T}{C_2}\right)\left[1-\frac{1}{2}\left(\frac{C_2(P-m+3)}{Tq}\right)+\frac{1}{12}\left(\frac{C_2(P-m+3)}{Tq}\right)^2\right.$$

$$\left.-\frac{1}{720}\left(\frac{C_2(P-m+3)}{Tq}\right)^4+\frac{1}{30240}\left(\frac{C_2(P-m+3)}{Tq}\right)^6\right.$$

$$\left.-\frac{1}{1209600}\left(\frac{C_2(P-m+3)}{Tq}\right)^8+\cdots\cdot\right] \tag{7}$$

$$L\fallingdotseq\sum_{m=0}^{\infty}A\cdot B_m\cdot C_1\frac{\Gamma(P-m+3)}{q^{P-m+3}}\cdot\frac{1}{\exp\left[\dfrac{C_2(P-m+3)}{Tq}\right]-1}$$

Since $C_2(P-m+3)/Tq>4\sim5$ from Table 1

$$L\fallingdotseq\sum_{m=0}^{\infty}A\cdot B_m\cdot C_1\frac{\Gamma(P-m+3)}{q^{P-m+3}}\cdot\exp\left[-\frac{C_2(P-m+3)}{Tq}\right] \tag{8}$$

As the result, we obtain the color stimulus value L_0 for a bare light source

$$L_0=\int_V^R E_\lambda\bar{S}_\lambda d\lambda=A\cdot C_1\cdot\frac{\Gamma(P+3)}{q^{P+3}}\cdot\exp\left[-\frac{C_2(P+3)}{Tq}\right] \tag{9}$$

Thus, when a light source is not influenced by the object color, $1/T$ dependence of the color stimulus value is approximately represented by an exponential function at least under the assumed conditions.

2.2 Tristimulus values of object color.

Tristimulus values X, Y, Z, of an object are defined as the ratios of L to the stimulus value of the light source Y_0.

$$X=\frac{\int_V^R E_\lambda\bar{x}_\lambda\rho_\lambda d\lambda}{\int_V^R E_\lambda\bar{y}_\lambda d\lambda};\quad Y=\frac{\int_V^R E_\lambda\bar{y}_\lambda\rho_\lambda\rho\lambda}{\int_V^R E_\lambda\bar{y}_\lambda d\lambda};\quad Z=\frac{\int_V^R E_\lambda\bar{z}_\lambda\rho_\lambda d\lambda}{\int_V^R E_\lambda\bar{y}_\lambda d\lambda} \tag{10}$$

Since coefficients of $\bar{y}$ are equal in (8) and (9), Y of (10) can be written as follows.

$$Y=B_0+B_1\exp\left[C_2/Tq_y\right]+B_2\exp\left[2C_2/Tq_y\right]+B_2\exp\left[3C_2/Tq_y\right]+\cdots\cdot \tag{11}$$

which can be expanded as below, for $\exp(C_2/Tq_y)$ in (11) is nearly equal to unity and m is small, Thus by taking the first terms only, we have

$$Y\fallingdotseq(B_0+B_1+B_2+B_3+\cdots\cdot)+\frac{1}{T}D(B_1+2B_2+3B_3+\cdots\cdot)$$

$$+\frac{1}{2}\left(\frac{1}{T}\right)^2D^2(B_1+4B_2+9B_3+\cdots\cdot) \tag{12}$$

where $C_2/q_y=D$.

From these considerations, it is expected that, the tristimulus values of reflected color of an object of known spectral reflection characteristics show ayproximately linear dependence upon reciprocal color temperature.

Table 2. Values of the constants in empirical equations

$(M=1/T\times10^6)$	$X=a_x+b_x\cdot M+c_x\cdot M^2$				$Y=a_y+b_y\cdot M$			$Z=a_z+b_z\cdot M+c_z\cdot M^2$			
Samples	a_x	b_x	c_x	errors ± (%)	a_y	b_y	errors ± (%)	a_z	b_z	c_z	errors ± (%)
1- 7-17	41.50	0.00336	0.000160	0.01	27.89	0.03550	0.03	49.02	−0.19070	0.000207	0.03
1- 7-15	24.87	0.01903	0.000092	0.02	16.05	0.02743	0.06	25.43	−0.09312	0.000094	0.02
1- 7-13	12.47	0.00756	0.000047	0.02	8.21	0.01205	0.03	14.29	−0.05508	0.000057	0.01
1-10-14	21.14	0.01429	0.000113	0.04	10.26	0.03073	0.03	12.86	−0.04741	0.000043	0.02
2- 8-16	36.04	0.02581	0.000134	0.08	22.69	0.04183	0.01	27.27	−0.10710	0.000121	0.03
2- 8-14	19.40	0.03414	0.000058	0.03	13.06	0.02505	0.02	14.73	−0.06281	0.000078	0.04
3- 7-17	36.91	0.04843	0.000078	0.04	30.35	0.03475	0.05	33.89	−0.12234	0.000117	0.04
3- 7-14	17.65	0.00468	0.000078	0.02	11.39	0.01877	0.04	10.25	−0.03492	0.000030	0.02
4- 5-18	43.38	0.06523	0.000035	0.02	42.55	0.03016	0.06	54.49	−0.21094	0.000234	0.04
4- 5-13	7.60	0.03028	−0.000020	0.02	8.18	0.00936	0.02	10.87	−0.04604	0.000055	0.02
5- 6-17	38.22	0.04602	0.000089	0.04	32.83	0.03625	0.00	19.62	−0.07872	0.000092	0.00
5- 6-16	23.77	0.02250	0.000062	0.03	21.28	0.02183	0.05	16.69	−0.05562	0.000043	0.01
6- 5-18	43.69	0.06828	0.000054	0.05	45.90	0.03333	0.04	29.99	−0.09922	0.000086	0.03
6- 5-17	33.06	0.05109	0.000039	0.05	33.53	0.02708	0.04	23.53	−0.09875	0.000125	0.02
7- 5-19	55.58	0.04296	0.000101	0.04	61.33	0.02360	0.02	49.71	−0.17312	0.000156	0.03
7- 5-17	34.99	0.02602	0.000089	0.03	35.64	0.02216	0.05	18.30	−0.06156	0.000047	0.02
8-14- 1	62.85	−0.00672	0.000117	0.01	65.38	0.00738	0.02	127.54	−0.50984	0.000586	0.18
9- 4-19	52.17	0.01140	0.000117	0.02	66.09	0.00330	0.03	59.14	−0.19794	0.000179	0.05
10- 4-19	46.41	0.00656	0.000078	0.05	60.49	−0.00145	0.02	74.60	−0.27312	0.000281	0.09
10- 5-18	31.55	0.00820	0.000055	0.03	46.63	−0.00710	0.03	34.78	−0.12538	0.000129	0.06
11- 5-18	30.04	−0.00300	0.000050	0.01	44.81	−0.01477	0.03	54.17	−0.19859	0.000211	0.03
11- 5-15	10.70	0.00008	0.000011	0.00	17.29	−0.00616	0.01	17.67	−0.05796	0.000554	0.01
12-19- 4	47.30	−0.02028	0.000095	0.02	60.55	−0.01983	0.04	107.93	−0.41281	0.000453	0.07
13- 6-15	19.47	−0.00347	0.000004	0.01	34.58	−0.02291	0.03	65.15	−0.24734	0.000273	0.12
13- 6-15	10.20	−0.00817	0.000011	0.00	19.15	−0.01497	0.04	34.48	−0.11757	0.000113	0.05
14- 6-17	23.06	−0.02987	0.000043	0.02	32.09	−0.02546	0.02	79.96	−0.29294	0.000304	0.05
15- 7-15	17.78	−0.03804	0.000043	0.01	19.90	−0.01806	0.02	77.82	−0.30031	0.000328	0.07
16- 6-16	30.27	−0.06144	0.000084	0.05	26.92	−0.01708	0.04	115.34	−0.41812	0.000406	0.23
17- 5-16	31.36	−0.06100	0.000087	0.03	24.09	−0.01090	0.01	120.42	−0.46296	0.000492	0.11
18- 6-12	16.37	−0.04525	0.000050	0.02	6.56	−0.00186	0.02	80.86	−0.33000	0.000375	0.20

19- 5-12	15.81	−0.04319	0.000063	0.01	7.12	−0.00298	0.02	60.93	−0.24075	0.000258	0.06
20- 5-12	11.13	−0.02468	0.000034	0.01	3.59	−0.00173	0.01	45.09	−0.18306	0.000199	0.11
21- 5-16	32.34	−0.02241	0.000080	0.05	21.31	0.00842	0.04	103.11	−0.41187	0.000468	0.06
22- 6-13	15.27	0.00546	0.000033	0.17	8.65	−0.01175	0.01	45.42	−0.17344	0.000172	0.02
23- 7-15	27.33	−0.00422	0.000117	0.02	14.19	0.02475	0.04	53.14	−0.21281	0.000234	0.12
24-19- 5	64.16	−0.01107	0.000148	0.05	56.17	0.01703	0.05	140.84	−0.55638	0.000614	0.25

					$Y=a_y+b_y\cdot M+c_y\cdot M^2$							
Samples	a_x	b_x	c_x	errors ±(%)	a_y	b_y	c_y	errors ±(%)	a_z	b_z	c_z	errors ±(%)
P. B. Blue 3*R*	35.49	−0.10539	0.000129	0.03	23.10	−0.02420		0.03	166.21	−0.62656	0.000640	0.32
E. Green *B* Supra	36.35	−0.06492	0.000074	0.02	54.64	−0.04400		0.05	115.36	−0.43687	0.000468	0.10
O. Violet 3*R*	25.99	−0.02989	0.000136	0.02	8.46	0.01875		0.06	72.46	−0.27765	0.000289	0.09
Fuchsin Red	46.56	−0.02703	0.000195	0.05	14.17	0.04308		0.11	120.10	−0.50031	0.000578	0.07
Malachitgrün	23.22	−0.05281	0.000047	0.03	41.45	−0.04848		0.06	100.78	−0.33219	0.000297	0.07
Rhrdamin *B* Conc	56.63	−0.02096	0.000154	0.05	30.51	0.00367	0.000050	0.01	178.54	−0.68969	0.000734	0.13
O. Blue 2*GW*	15.18	−0.05097	0.000061	0.01	13.27	−0.01573		0.02	75.04	−0.29734	0.000336	0.05
O. Orange *GRW*	59.00	0.01672	0.000195	0.05	47.51	0.05383		0.06	18.35	−0.06770	0.000063	0.02
F. Orange *G*	65.04	0.03367	0.000144	0.04	78.77	0.01440		0.05	46.73	−0.15898	0.000152	0.03
T—*R*	36.96	−0.01354	0.000068	0.05	39.48	0.00445	−0.000019	0.01	90.32	−0.35295	0.000382	0.14

P. B. Blue 3*R*=Polar Brilliant Blue 3*R* 160: E. Green *B* Supra=Erio Green *B* Supra
O. Violet 3*R*=Orasol Violet 3*R*: O. Blut 2*GW*=Orasol Blue 2*GW*
O. Orange *GRW*=Orasol Orange *GRW*: F. Orange *G*=Fat Orange *G*

Table 3. Chromaticity coodinates for the colors in standard illuminant (C)

Samples	x	y	Y	Samples	x	y	Y
1— 7—17	0.436_8	0.320_1	33.3_3	13— 6—17	0.228_7	0.367_9	31.3_9
1— 7—15	0.466_0	0.317_5	20.3_3	13— 6—15	0.203_3	0.373_7	17.4_6
1— 7—13	0.454_7	0.313_2	10.1_0	14— 6—17	0.216_9	0.305_9	27.9_9
1—10—14	0.538_7	0.315_1	14.8_6	15— 7—15	0.183_9	0.244_4	17.2_6
2— 8—16	0.496_9	0.340_5	29.3_6	16— 6—16	0.209_7	0.219_7	24.4_9
2— 8—14	0.520_9	0.336_6	16.7_3	17— 5—16	0.221_3	0.203_8	22.4_9
3— 7—17	0.459_1	0.354_1	35.5_6	18— 6—12	0.189_8	0.115_0	6.5_7
3— 7—14	0.495_6	0.355_3	14.1_6	19— 5—12	0.220_8	0.136_9	6.7_0
4— 5—18	0.416_7	0.362_6	47.1_9	20— 5—12	0.237_6	0.113_0	3.9_3
4— 5—13	0.441_7	0.359_8	9.6_3	21— 5—16	0.293_4	0.212_6	22.6_8
5— 6—17	0.492_8	0.401_7	38.0_6	22— 5—16	0.335_5	0.202_0	10.4_6
5— 6—16	0.455_0	0.393_4	24.7_3	23— 7—15	0.396_0	0.242_6	18.4_6
6— 5—18	0.447_0	0.410_6	50.8_8	24—19— 4	0.337_1	0.299_9	58.7_9
6— 5—17	4.458_4	0.413_5	37.6_3	P. B. Blue $3R$	0.172_4	0.153_4	20.2_0
7— 5—19	0.408_5	0.413_1	64.8_6	E. Green B Supra	0.206_2	0.349_2	48.5_8
7— 5—17	0.453_7	0.435_1	39.1_6	O. Violet $3R$	0.333_4	0.152_8	11.3_0
8—14— 1	0.329_2	0.339_1	66.6_2	Fuchsin Red	0.366_6	0.165_1	21.0_3
9— 4—19	0.358_3	0.423_4	66.6_9	Malachitgrün	0.151_9	0.312_0	34.2_0
10— 4—19	0.331_7	0.397_7	59.0_2	Rhodamin B Cone	0.311_7	0.176_1	32.2_0
10— 5—18	0.343_8	0.460_9	45.5_6	Orasol Blue $2GW$	0.154_0	0.188_9	11.0_4
11— 5—18	0.298_9	0.413_4	42.6_6	O. Orange GRW	0.499_8	0.424_4	55.5_8
11— 5—15	0.289_6	0.432_7	16.3_9	Fat Orange G	0.404_1	0.450_4	80.9_6
12—19— 4	0.290_4	0.355_1	57.1_9		0.296_6	0.323_6	39.7_6

P. B. Blue $3R$=Polar Briliant Blue $3R$ 160%: E. Green B Supra=Erio Green B Supra
O. Violet $3R$=Orasol Violet $3R$: O. Orange GRW=Orasol Orange GRW

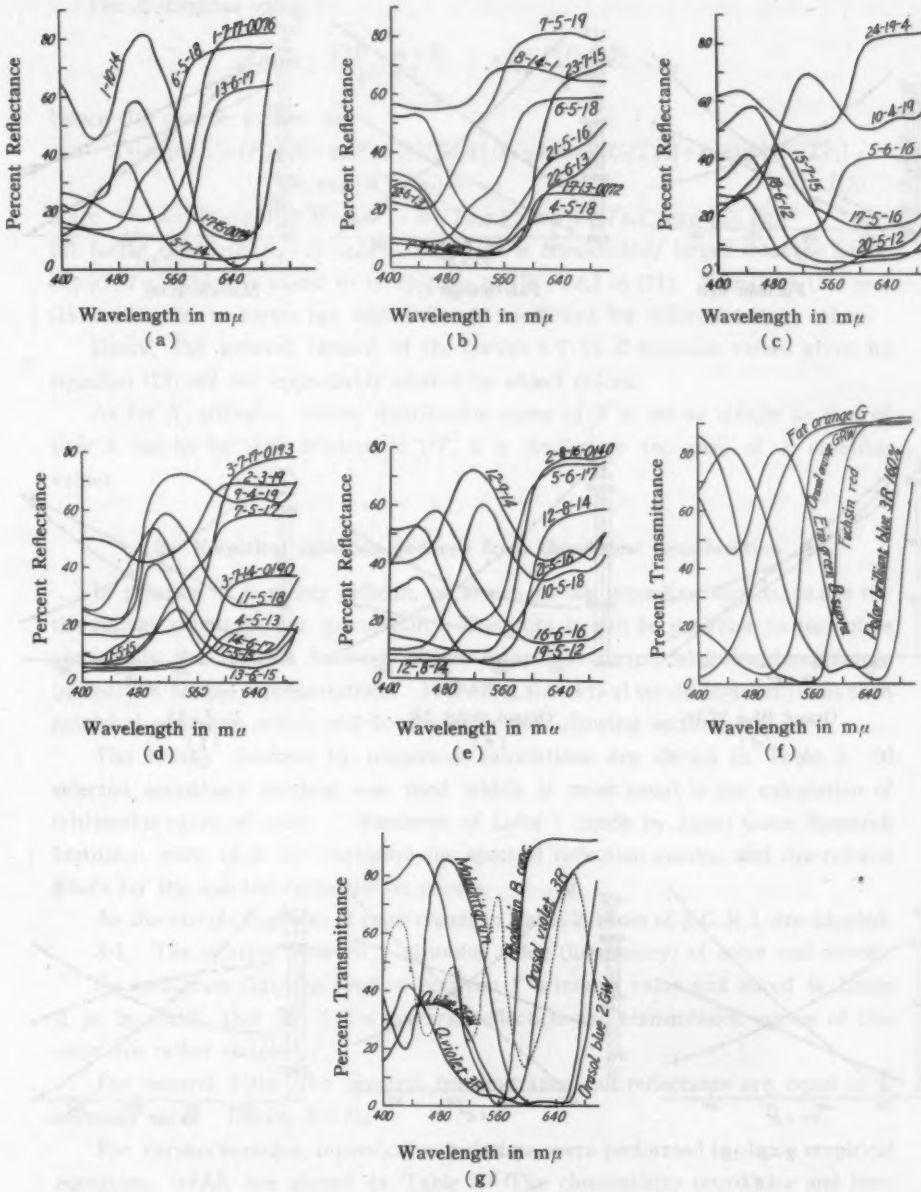

Fig. 2. Spectral transmission and reflection curves of samples.

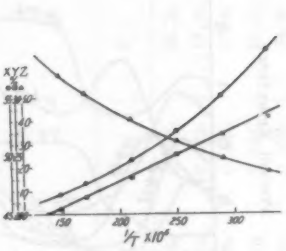

Fuchsin Red
(a)

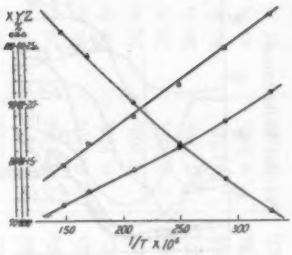

Fat Orange *G*
(b)

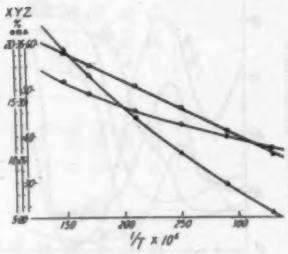

Malachitgrun
(c)

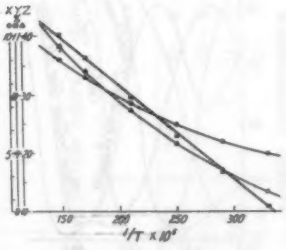

Orasol Blue 2*GW*
(d)

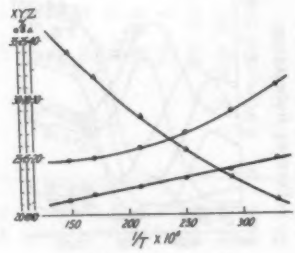

Orasol violet 3*R*
(e)

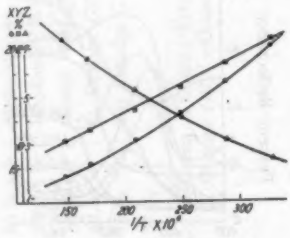

1—7—13
(f)

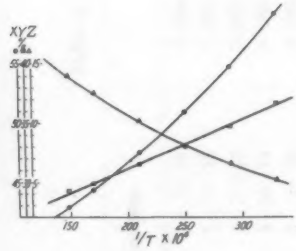

2—8—16
(g)

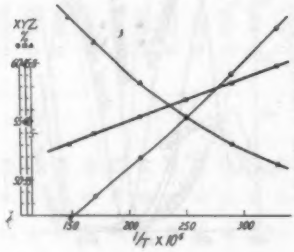

5—6—17
(h)

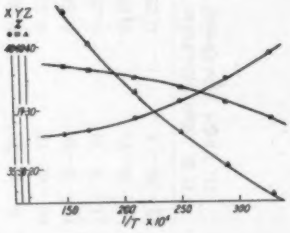

T—*R*
(i)

Fig. 3. Relation between tristimulus values and mired.

For Z stimulus value,

$$A \cdot B_m \cdot C_1 \frac{\Gamma(P-m+3)}{q^{P-m+3}} \Big/ A \cdot C_1 \frac{\Gamma(P_y+3)}{q^{P_y+3}} = k_m$$

Hence (10) can be written as

$$Z = \exp[C_z\{q_z(P_y+3)-q_y(P_z+3)\}/Tq_yq_z[(k_0+k_1\exp[C_2/Tq_z]+k_2\exp[2C_2/Tq_z] + k_3\exp[3C_2/Tq_z]+\cdots\cdots \quad (13)$$

Since $\exp[C_2\{q_z(P_y+3)-q_y(P_z+3)\}/Tq_yq_z] > \exp[C_2/Tq_y] > \exp[C_2/Tq_z]$

the factor $\exp[C_2\{q_z(P_y+3)-q_y(P_z+3)\}/Tq_yq_z]$ is considerably larger than the factor $\exp[C_2/Tq_z]$ which is closer to unity than $\exp[C_2/Tq_y]$ in (11). Equations (11) and (13) are similar in forms but with different coefficient for different object colors.

Hence, the general feature of the curves $1/T$ vs Z stimulus values given by equation (13) are not appreciably altered by object colors.

As for X stimulus values, distribution curve of $\bar{x}$ is not as simple as that of $\bar{y}$ or $\bar{z}$, but as for their relation to $1/T$, it is similar to the case of Z stimulus values.

3. Empirical equation deduced from theoretical consideration

In practice, it is rather difficult, as shown in the preceding section, to use the theoretical equations for calculation. Therefore it will be desirable to formulate empirically the relation between object color and reciprocal color temperature (mired)* in simple representations. Preceding theoretical condsideration yields such empirical equations which will be shown in the following sections.

The results obtained by numerical calculations are shown in Table 2. 30 selected coordinate method was used which is most usual in the calculation of tristimulus values of color. "Standards of Color" (made by Japan Color Research Institute) were used for obtaining the spectral reflection curves, and dye-colored filters for the spectral transmission curves.

As the sample numbers of color charts in Table 2, those of J. C. R. I. are adopted.

3. 1. The relation between Y stimulus value (luminosity) of color and mired.

As seen from (12), the relation between Y stimulus value and mired is linear if m is small, that is, if the spectral reflection and transmission curves of this color are rather simple.

For neutral filter, the spectral transmittance and reflectance are equal to Y stimulus value. Hence, $Y = B_0$.

For various samples, numerical calculations were performed to obtain empirical equations, which are shown in Table 2. The chromaticity coordinate and lum-

* Micro reciprol degree

inosity of the samples under irradiation of standard illuminant "C" are shown in Table 3.

In Table 2, standard deviations are given in the last column. Fig. 3 shows the relation between tristimulus values and mired.

Linear dependence of luminosity upon mired was verified for several special samples.

For reflected color such as that given in color charts, this linearity was ascertained for all the samples.

Dotted curve in Fig. 2g is the one that was calculated by assuming m to be large. This is represented by a quadratic equation.

3.2. The relation between X, Z stimulus values of color and mired.

We have noted before that the relation between Z stimulus value and mired, (13), is not appreciably altered by the difference colors of objects. Hence, in a limited range of color temperature, the quadratic forms can be used with a sufficient degree of accuracy. They are shown in Table 2.

Although $\bar{x}$ distribution coefficients in the X, Y, Z system are more complicated in this case, the relations between X stimulus value and mired are similar to the case of Z stimulus value.

For example, for a blue or green colored object, $\bar{x}$ distribution coefficients are predominantly effective only in a short wave length region, and for red or orange object, only in a long wave length region.

For the intermediate color, though $\bar{x}$ distribution coefficients must be taken into account for the whole visible wave length region, substantial alteration should not occur in the relation between X stimulus value and mired.

Therefore the quadratic formulae are also applicable, which are also shown in Table 2.

3.3. Empirical equations and their applications.

As shown in Table 2, the relation between mired and tristimulus values of various colors are represented by the following empirical equations:

$$X=a_x+b_xM+C_xM^2 \qquad x=\frac{a_x+b_xM+C_xM^2}{A+BM+CM^2}$$

$$Y=a_y+b_yM+C_yM^2$$

$$Z=a_z+b_zM+C_zM^2 \qquad y=\frac{a_y+b_yM+C_yM^2}{A+BM+CM^2}$$

where coefficients a, b and c are characteristics of each of the colors, since $M=1/T\times10^6$, $A=a_x+a_y+a_z$, $B=b_x+b_y+b_z$, $C=c_x+c_y+c_z$. Applying these equations, color stimulus values and chromaticity coordinates are easily calculated for any color temperature.

In practical calculations, tristimulus values for "A", "B" and "C" standard

illuminant sources are numerically calculated at first by the usual 30 selected coordinate method using colorimetric computer, thereby the coefficients are determined.

4. Summary

The relation of tristimulus values of color and color temperature of a light source was discussed with the conclusion, that (in the color temperature region between "*A*" and "*B*" standard illuminant sources) this relation is represented by an exponential form which was verified for various color samples at least within the accuracy of numerical calculation.

By determining tristimulus values of an object color for "*A*", "*B*" and "*C*" standard illuminant sources by the empirical equation obtained and then by calculating empirically coefficients for this color, color stimulus values can be obtained for any color.

Acknowledgements

The writer wishes to thank Assistant Prof. M. Kamiyama, Assistant Prof. R. Hioki and Mr. S. Jinbo for their kind advice and Mr. T. Saito and Miss K. Miura for their help in calculation.

CONTENTS

Properties of Pneumatic Infra-red Dectector (I) ..... K. YOSIHARA 67

On the Measurement of Response Function from the Contrast of Chart.....
..... T. OSE 85

Arc Spectra of Pure Aluminum in Various Gases ..... M. SHIMAUCHI 101

On the Relation Between Tristimulus Values of Color and Color Temperature
of Planckian Radiation ..... M. HARADOME 112